THE UNIVERSITY OF CHICAGO

SPONTANEOUS PATTERNING VIA FRONTAL POLYMERIZATION

A DISSERTATION SUBMITTED TO

THE FACULTY OF THE PRITZKER SCHOOL OF MOLECULAR ENGINEERING

IN CANDIDACY FOR THE DEGREE OF

DOCTOR OF PHILOSOPHY

BY

MASON ALLEN DEARBORN

CHICAGO, ILLINOIS

MARCH 2023

Table of Contents

List of Tables

List of Figures

Acknowledgements

I am very grateful to have been part of the Esser-Kahn group during my graduate studies both at the University of Chicago. To my PhD advisor, Prof. Aaron Esser-Kahn for the opportunity to join your group, and for your exceptional support and guidance all these years. Thank you for teaching me how to become a better scientist and professional.

To the candidacy and thesis committee members, Prof. Paul Nealey and Prof. Shrayesh Patel, for their support and helpful discussions about my research.

To my friends from graduate school for walking with me through this challenging path, and for all the support and fun times we have shared together.

To the rest of the Esser-Kahn group, past and present members that I have had the pleasure of knowing all these years. I enjoyed spending time with you and learning from you.

To the funding agencies, especially the National Science Foundation (NSF) and the Air Force Office of Scientist Research (AFOSR) for their generous financial support for all these research projects.

And last but not least, to my parents, my sisters, my family, my girlfriend, and friends for their unconditional love, friendship, and support. I would not have made it this far without you.

Abstract

Traditional composite manufacturing is a multi-step process limited to fabrication of uniform parts with a high time and energy cost. Patterning of materials with spatial control of mechanical properties would enable fabrication of more complex parts with unique functionality for applications beyond what is currently possible. Reaction-diffusion processes have demonstrated potential for creating patterned materials and are herein explored within an advanced method of fabricating high-performance polymeric materials and composites – frontal polymerization. Frontal polymerization (FP) uses a self-propagating exothermic reaction wave to create thermosetting polymeric and composite parts with zero energy input after simple thermal initiation without sacrificing mechanical properties, offering an alternative to traditional autoclave curing. Currently, FP is only used to create parts with uniform properties throughout, limiting the applicability of fabricated parts. The work reported herein develops tools for modulating reaction-diffusion patterning for spatial control of mechanical properties across parts fabricated via the frontal ring-opening metathesis polymerization (FROMP) of dicyclopentadiene (DCPD) and 1,5-cyclooctadiene (COD), enabling more advanced designs in one processing step.

Videos and infrared videos (Movies S1-11) showing the propagation of fronts in Chapters 2 and 4 were provided outside this document as supplementary files.

Chapter 1: Introduction and Background

1.1 Overview of frontal polymerization

Frontal polymerization (FP) is a directional polymerization process in which an initial thermal or photo stimulus induces a localized reaction zone, triggering an exothermic polymerization which releases energy to further initiate polymerization events at the boundary between polymer and unreacted monomer. The reaction zone thus propagates in a wave, called the "polymerization front." This reaction front is fueled by the thermal diffusion of the exothermic heat of polymerization of monomer, producing fully-cured polymeric thermosets and thermoplastics with no energy input following the initial stimulus.

An analogy may be made to another self-propagating reaction, combustion. A spark serves as initial stimulus, materials with chemical potential react, releasing heat and light. This heat and light triggers adjacent combustion, spreading and thus amplifying energy released far beyond that of the spark. Rather than the destruction of material, frontal polymerization converts its fuel, monomer, into polymeric parts with desirable mechanical properties. Herein, we study a liquid mixture forming itself into a solid high-performance polymer.

Frontal polymerization was discovered in 1972 at the Institute of Chemical Physics in Chernogolovka, Russia,[1] when Chechilo *et al* demonstrated the self-perpetuating radical polymerization of methyl methacrylate. Initiation required >3500 atm of pressure in sealed reactors – too intense for widespread practical implementation. Research into frontal polymerization remained within the USSR until its fall in 1991, when Pojman rediscovered FP in 1991, demonstrating radical polymerization of methacrylic acid with benzoyl peroxide.[2] Pojman has authored over 150 publications on frontal polymerization and reviewed the field in 1996 and

2012.[3,4] Frontal polymerization has expanded to a wide array of chemistries and applications.[5–7] Three main modes of FP have been demonstrated. First, in photofrontal polymerization the front is driven by a continuous flux of radiation, most commonly UV light.[8–13] Second, isothermal frontal polymerization (IFP) utilizes the 'gel effect' to create a localized reaction zone to propagate slowly from a polymer seed. Finally, thermal FP is by far the most versatile and well-studied, and it involves the coupling of thermal transport and the Arrhenius dependence of the reaction rate of an exothermic polymerization. Photofrontal polymerization is limited by the penetration depth of light and photobleaching of initiator and IFP is limited in its speed (1 cm/day front velocity) and fabricable part size (~1 cm total front distance traveled).[12] Thermal FP is employed in this work and will be discussed here on.

Frontal polymerization may be utilized for any exothermic monomer with sufficiently high energy density such that heat generated exceeds heat lost to the environment. As well, the system must have sufficiently high activation energy such that the rate of reaction at the initial temperature is much lower than the rate of reaction at the front temperature.[3,5] A FP system must have sufficiently long "pot life," defined as the duration between the mixing of reactive components and the time at which FP can no longer occur due to decomposition or reaction of the reagents. High activation energy suppresses spontaneous polymerization prior to desired initiation, informing initiator and monomer selection. Much early work employed free-radical frontal polymerization, with its wide array of amenable exothermic monomers, to study the effect of reactor geometry, initiator concentration, viscosity, and other factors on FP. However, volatile byproducts from radical initiators remain trapped in the material and create voids unless an impractically high pressure is used, limiting the resulting polymer's mechanical properties. Mariani et al introduced alternate initiator systems, but they suffered from short pot life.[14] FP of

epoxy was studied in an effort to make mechanically robust polymers, and Chekanov et al produced FP epoxies comparable in thermal and mechanical properties to those conventionally cured.[15] Similar to the approach taken in chapters 2 and 3, Frulloni developed a numerical computational model of FP that could accurately predict frontal velocity and temperature.[14] Methods such as pairing a radical initiation system and a cationic curing system and decreasing initiator concentration were demonstrated, but FP of epoxy remains limited to either having short pot life or requiring high temperature conditions.[16–18]

1.2 Frontal polymerization of dicyclopentadiene (DCPD)

Within the library of materials synthesized via FP, recent efforts have turned to creating high-performance materials for structural applications. The application of FP to composite manufacturing has enormous demonstrated potential, as FP uses the enthalpy of polymerization rather than an external energy source.[5] Current composite fabrication requires an energy- and time-intensive autoclave curing process after significant upfront capital investment.[19] With proper enabling chemistries for monomer and activation, the environmental and financial burdens that currently inhibit more broad application of composites could be alleviated by taking advantage of FP's rapid polymerization with zero-energy input following initiation. Curing by FP of a thermoset polymer and carbon fiber-reinforced polymer composites was recently demonstrated by a collaboration of Groups at the University of Illinois. In these works, the frontal ring-opening metathesis polymerization (FROMP) of dicyclopentadiene (DCPD) was used to create thermosets and polymeric composites without sacrificing mechanical properties relative to traditionally cured epoxy-based composites.[20,21] This research was made possible by chemical advancements, especially in using the alkyl phosphite inhibitor (tributyl phosphite,

TBP) for extending the pot life to over thirty hours for a large processing window after combination of the reagents. Due to FP, this was completed with a reduction of up to ten orders of magnitude in energy consumed and of up to two orders of magnitude in time to cure.[20] The work reported herein was in collaboration with these groups and builds upon these chemistries by adding patterning to this system for creating high-performance materials.

1.3 Morphogenic manufacturing

Manufacturing today is optimized for the fabrication of uniform parts, progressing with incremental improvements in new material systems, more efficient manufacturing processes, and decreased irregularities within the parts that act as points of failure for crack propagation to begin. At their most advanced, composite structural materials are currently designed as uniform individual parts to be assembled into a complex greater structure. For example, in a carbon fiber-reinforced polymer composite, two phases of material are fabricated separately before being combined. Carbon fibers confer strength under tension to the completed part and are placed within a thermoset polymer matrix that confers strength under compression. Together, this yields remarkable strength relative to the weight of the part. This has two major limitations. First, composite failure often occurs at the interface between the two phases, such as fiber pullout. Second, much of the expense that constrains composites to high-value items comes from combining and binding together each of the separately manufactured parts. Structures and patterns are then added in multistep manufacturing processes, such as layer-by-layer assembly,[22] lithography,[23] or molding and casting. The speed and energy-efficiency of frontal polymerization from the enabling advances in FP of DCPD discussed in the previous section only allow us to make the same parts, cured in a better way. A revolutionary shift in the manufacturing paradigm

would require systems that can form themselves in one step from initial homogeneity, autonomously generating the spatial variation in mechanical properties that yield the improved performance of composite performance.

Beyond improving efficiency in fabricating existing materials, the reaction-diffusion system of FP will be explored for making unique materials with patterning achieved during the one-step fabrication. Reaction-diffusion (RD) systems were first presented as a mathematical explanation for patterning of biological systems by Alan Turing in his seminal paper on morphogenesis.[24,25] Morphogenesis is the biological process of shape formation, describing the physical forces that control the organized spatial distribution of cells during embryo development and many other processes in mature organisms. In these systems, symmetry-breaking events disrupt initially homogeneous systems and create order determined by the coupling of diffusion and reaction of its components. From these initially uniform systems, emergent pattern formation is dictated by the relative rates of reaction and diffusion of an activator and inhibitor, called "morphogens."[26,27] Together, these create nonlinear dynamic systems with a short-range positive feedback and a long-range negative feedback, defining the formation of complex patterns.[28,29] Nature uses many RD processes to build and control structures at all lengthscales. Examples include intracellular signaling with calcium waves,[30] synchronization of neuron firing in the brain,[31,32] skin patterns in many animals like zebras,[33,34] and even the formation of spiral stellar disk structures in isolated galaxies.[35] Grzybowski *et al* reviewed applications of RD to micro- and nanotechnology in 2005, advocating for the application of RD as a programmable, single-step process capable of patterning. They present a massive design space for manipulating RD systems to form patterns of desired structures and properties. Levers for tunability include the parameters of the reaction kinetics, relative diffusivities of morphogens, mediums, substrates,

initiation mechanism, external fields, and more. However, many RD patterns are transient, existing temporarily in soft materials, whereas static patterns in structural solids are desired for macro-scale applications such as composites. Toward that end, Gryzbowski *et al* demonstrated using RD processes to form micropatterned hydrogel stamps to be soaked in reagents that etched the patterns into a solid substrate, such as a thin metal or glass film potential applications in sensing and electronics. The 2-dimensionality of these patterns and additional stamping step limit practical application to morphogenic manufacturing.[36]

Frontal polymerization is a particularly exciting reaction-diffusion system, defined by the coupling of Arrhenius reaction kinetics and thermal diffusion. This system is expressed by the 1D thermochemical equations to the right, where α and T are the degree of cure and temperature, respectively, H_R is the heat of reaction, and κ, ρ, and c_p denote the thermal conductivity, density, and heat capacity of the material, respectively. The first equation encompasses the heat generated by the reaction, and the second describes the evolution of degree of cure in the cure kinetics model.[20]

$$\begin{cases} \kappa\left(\frac{\partial^2 T}{\partial x^2}\right) + \rho H_{\mathrm{r}} \frac{\partial \alpha}{\partial t} = \rho C_{p,\mathrm{r}} \frac{\partial T}{\partial t}, \\ \frac{\partial \alpha}{\partial t} = f(\alpha, T). \end{cases}$$

(1)

This work aimed to extend the principles of RD to manufacturing, using the Arrhenius reaction kinetics of FROMP and the thermal diffusion of its heat. This autonomous pattern formation from initially homogeneous systems offers a mechanism for spatial control of mechanical properties during fabrication. This is achieved as spatial variation in heating as controlled by the interplay of

feedbacks in the RD system translates directly to the final mechanical properties between regions of the part cured at different temperatures. Per the second equation in the frontal RD equations presented above, cure kinetics are temperature-dependent, and degree of cure determines the properties of the fabricated part.[5,37,38] Furthermore, thermal diffusion in FP occurs orders-of-magnitude faster than the mass diffusion most commonly coupled with reaction in RD systems, and the polymerization may yield robust polymer networks rather than phases of high concentration of small molecules in soft materials. Using the ideal manufacturing mechanisms of nature, novel polymeric structures and materials may thus be created in a single, efficient processing step with emergent order through autonomous morphogenic patterning.

1.4 Modulating frontal profile

Necessary in realizing the morphogenic manufacturing potential of frontal polymerization is the predictable and controlled divergence from uniform frontal propagation. Heat transfer at the front, defined by front position, velocity, and temperature ("frontal profile"), governs the final degree-of-cure of the polymer, and thereby its mechanical performance. Thermal instabilities in the propagation of the front, overlap of multiple fronts, and obstacles or additives in the path of the front lead to spatial variation in the frontal profile. These phenomena have previously been studied with the intent to repress them for uniformity in fabrication; however, they are employed to spontaneously generate patterns in this work.

1.4.1 Frontal overlap

Initiating two fronts to propagate in the FP of DCPD was demonstrated by Yourdkhani *et al* to reduce fabrication time, which is a function of front velocity and the traveling distance of

the front.[39] Thermally triggering two fronts simultaneously at opposite ends of a sample halved the time to fully cure; however, as the two fronts merge, the heat produced in opposite fronts cannot be absorbed by unreacted monomer ahead of the front. This led to a thermal spike well above the maximum temperature the front achieves when propagating in space, and they observed volume changes, variation in material properties, or creation of residual stresses in the region along the high temperature-cured line of frontal collision. While undesirable for uniform curing, this creates the capacity for domains of distinct properties to form themselves during FP, enabling spontaneous patterning. A tool capable of the modulation of the properties within and size and location of these domains did not exist. We manipulate the collision of two fronts to take advantage of the mechanical property variation caused by this thermal spike in Chapter 2. In Chapter 4, we lay the groundwork for initiating at a high number of locations for increasing occurrences of frontal overlap, thus increasing the number of domains of material cured at different temperature in the pattern.

1.4.2 Thermal instabilities in frontal polymerization

Fronts do not always propagate as stable, planar fronts. Analogous to oscillating reactions and first observed in self-propagating high-temperature synthesis (SHS),[40] fronts can propagate periodically as "spin modes" or pulsations as the front exhibits swings between high and low temperature and velocity due to the competition between reaction and transport at the front.[41] Spin modes are most commonly observed in cylindrical reactors, where a hot spot forms and propagates around the reactor ahead of the front, leaving a helical pattern.[42] Pojman observed these in many systems and analyzed the linear stability of the single-head (one hot spot

propagating) spin-mode in detail with Ilyashenko.[43] They demonstrated the linear stability of front propagation in adiabatic cylindrical reactors is governed by the Zeldovich number (Z):

$$Z = \frac{T_m - T_0}{T_m} \frac{E_{eff}}{RT_m} \quad (2)$$

Extending the Zeldovich number from combustion and other single reactions to FP, lowering the initial temperature (T_0), increasing the front temperature (T_m), and increasing the energy of activation (E_{eff}) all increase the Zeldovich number. The planar mode is stable if $Z < Z_{cr} = 8.4$, and higher spin mode instabilities can be observed above that stability threshold. Instabilities can be observed in FP systems with low energy density, high heat loss, or high activation energy, and the trends of the above inputs to Z used as a guide for quelling or inducing thermal instabilities in FP.[5]

In 2021, Lloyd *et al* at UIUC within our collaboration demonstrated the impact of initial temperature on instabilities generated in the FP of DCPD and cyclooctadiene (COD), an additional FROMP monomer. Lower T_0 led to less instability (gentler temperature spikes with more distance between them) in DCPD as expected; however, instabilities were inconsistent, not yet captured precisely enough for controlled patterning. This was especially true for COD, which propagated in the "chaotic" mode. Vital to the core idea of spontaneous generation of functional patterns, the patterned regions of DCPD had a 20 °C change in glass transition temperature and those in COD saw two orders of magnitude change in modulus.[41] The drastic front temperature spike-induced functional variation was key to our selection of DCPD and COD. In Chapters 2 and 3 we developed and experimentally validated computational models for FP of DCPD and

COD, respectively. Lloyd *et al*'s paper also contains theoretically achievable controlled patterned instabilities that my co-author of the work presented in Chapter 3 developed as an extension of our work.

1.5 References

(1) Khanukaev, B. B.; Kozhushner, M. A.; Enikolopyan, N. S.; Chechilo, N. M. Theory of the Propagation of a Polymerization Front. *Combustion, Explosion, and Shock Waves* **1974**. https://doi.org/10.1007/BF01463779.

(2) Pojman, J. A. Traveling Fronts of Methacrylic Acid Polymerization. *J. Am. Chem. Soc.* **1991**, *113* (16), 6284–6286.

(3) Pojman, J. A.; Ilyashenko, V. M.; Khan, A. M. Free-Radical Frontal Polymerization: Self-Propagating Thermal Reaction Waves. *Journal of the Chemical Society - Faraday Transactions* **1996**. https://doi.org/10.1039/ft9969202825.

(4) Pojman, J. A. 4.38 - Frontal Polymerization. In *Polymer Science: A Comprehensive Reference*; Matyjaszewski, K., Möller, M., Eds.; Elsevier: Amsterdam, 2012; pp 957–980. https://doi.org/10.1016/B978-0-444-53349-4.00124-2.

(5) Pojman, J. A. Frontal Polymerization. In *Polymer Science: A Comprehensive Reference, 10 Volume Set*; 2012. https://doi.org/10.1016/B978-0-444-53349-4.00124-2.

(6) Chekanov, Y. A.; Pojman, J. A. Preparation of Functionally Gradient Materials via Frontal Polymerization. *Journal of Applied Polymer Science* **2000**, *78* (13), 2398–2404.

(7) Nuvoli, D.; Alzari, V.; Pojman, J. A.; Sanna, V.; Ruiu, A.; Sanna, D.; Malucelli, G.; Mariani, A. Synthesis and Characterization of Functionally Gradient Materials Obtained by Frontal Polymerization. *ACS Applied Materials and Interfaces* **2015**. https://doi.org/10.1021/am507725k.

(8) Pearlstein, A. J. Criteria for the Absence of Thermal Convection in Photochemical Systems. *J. Phys. Chem.* **1985**, *89* (6), 1054–1058. https://doi.org/10.1021/j100252a033.

(9) A Pearlstein. The Onset of Convective Instability in a Triply Diffusive Fluid Layer. *Journal of Fluid Mechanics 202*, 443–465.

(10) Terrones, G.; Pearlstein, A. J. Effects of Optical Attenuation and Consumption of a Photobleaching Initiator on Local Initiation Rates in Photopolymerizations. *Macromolecules* **2001**, *34* (10), 3195–3204. https://doi.org/10.1021/ma001235y.

(11) Terrones, G.; Pearlstein, A. J. Diffusion-Induced Nonuniformity of Photoinitiation in a Photobleaching Medium. *Macromolecules* **2004**, *37* (4), 1565–1575.

(12) Cabral, J. Frontal Photopolymerization for Microfluidic Applications. *Langmuir* **2004**, *20* (23), 10020–10029.

(13) Pojman, J. A.; Downey, J. P. *Polymer Research in Microgravity*; American Chemical Society, 2001.

(14) Mariani, A.; Nuvoli, D.; Alzari, V.; Pini, M. Phosphonium-Based Ionic Liquids as a New Class of Radical Initiators and Their Use in Gas-Free Frontal Polymerization. *Macromolecules* **2008**, *41* (14), 5191–5196.

(15) Chekanov, Y. Frontal Curing of Epoxy Resins: Comparison of Mechanical and Thermal Properties to Batch-Cured Materials. *J. Appl. Polym. Sci.* **1997**, *66* (6), 1209–1216.

(16) Scognamillo, S., et al. Frontal Cationic Curing of Epoxy Resins in the Presence of Defoaming or Expanding Compounds. *J. Appl. Polym. Sci.* **2014**, *131* (11).

(17) Bomze, D.; et al. Radical Induced Cationic Frontal Polymerization as a Versatile Tool for Epoxy Curing and Composite Production. *J. Polym. Sci. Part A Polym. Chem.* **2016**, *54* (23), 3751–3759.

(18) Zhou, J.; et al. Fast Curing of Thick Components of Epoxy via Modified UV-Triggered Frontal Polymerization Propagating Horizontally. *Materials Letters* **2016**, *176*.

(19) Abliz, D.; Duan, Y.; Steuernagel, L.; Xie, L.; Li, D.; Ziegmann, G. Curing Methods for Advanced Polymer Composites -A Review. *Polymers and Polymer Composites* **2013**. https://doi.org/10.1177/096739111302100602.

(20) Robertson, I. D.; Yourdkhani, M.; Centellas, P. J.; Aw, J. E.; Ivanoff, D. G.; Goli, E.; Lloyd, E. M.; Dean, L. M.; Sottos, N. R.; Geubelle, P. H.; Moore, J. S.; White, S. R. Rapid Energy-Efficient Manufacturing of Polymers and Composites via Frontal Polymerization. *Nature* **2018**, *557* (7704), 223–227. https://doi.org/10.1038/s41586-018-0054-x.

(21) Ruiu, A.; Sanna, D.; Alzari, V.; Nuvoli, D.; Mariani, A. Advances in the Frontal Ring Opening Metathesis Polymerization of Dicyclopentadiene. **2014**, 2776–2780. https://doi.org/10.1002/pola.27301.

(22) Richardson, J. J.; Cui, J.; Björnmalm, M.; Braunger, J. A.; Ejima, H.; Caruso, F. Innovation in Layer-by-Layer Assembly. *Chem. Rev.* **2016**, *116* (23), 14828–14867. https://doi.org/10.1021/acs.chemrev.6b00627.

(23) THOMPSON, L. F. An Introduction to Lithography. In *Introduction to Microlithography*; ACS Symposium Series; AMERICAN CHEMICAL SOCIETY, 1983; Vol. 219, pp 1–13. https://doi.org/10.1021/bk-1983-0219.ch001.

(24) Campbell, C. J. *Adv. Mater.* **2004**, *16*, 1912–1917.

(25) Turing, A. M. *Philos. Trans. R. Soc. London* **1952**, *Ser. B* (237), 37–72.

(26) Turing, A. M. The Chemical Basis of Morphogenesis. *Bulletin of Mathematical Biology* **1990**. https://doi.org/10.1007/BF02459572.

(27) Grzybowski, B. A.; Bishop, K. J. M.; Campbell, C. J.; Fialkowski, M.; Smoukov, S. K. Micro- and Nanotechnology via Reaction-Diffusion. *Soft Matter*. 2005. https://doi.org/10.1039/b501769f.

(28) Pojman, J. A. Nonlinear Chemical Dynamics in Synthetic Polymer Systems. In *Chemomechanical Instabilities in Responsive Materials*; 2014; pp 221–240. https://doi.org/10.1007/s13398-014-0173-7.2.

(29) Datta, P.; Efimenko, K.; Genzer, J. The Effect of Confinement on Thermal Frontal Polymerization. *Polymer Chemistry* **2012**. https://doi.org/10.1039/c2py20640d.

(30) Bock, G. R. *Calcium Waves, Gradients and Oscillations*; Wiley & Sons, 1995; Vol. 188.

(31) Gray, C. M. *Nature* **1989**, *338*, 334–337.

(32) Terman, D. *Physica D* **1995**, *81*, 148–176.

(33) Jiang, T. X.; et al. *Int. J. Dev. Biol.* **2004**, *48*, 117–135.

(34) Kondo, S. *Genes Cells* **2002**, *7*, 535–541.

(35) Cartin, D. *Phys. Rev. E: Stat. Phys., Plasmas, Fluids, Relat. Interdiscip. Top.* **2002**, *65*, 16120.

(36) Bitner, A.; Grzybowski, B. A. *J. Phys. Chem. B* **2004**, *108*, 19904–19907.

(37) Goli, E.; Robertson, I. D.; Geubelle, P. H.; Moore, J. S. Frontal Polymerization of Dicyclopentadiene: A Numerical Study. *Journal of Physical Chemistry B* **2018**. https://doi.org/10.1021/acs.jpcb.7b12316.

(38) Pojman, J. A. Mathematical Modeling of Frontal Polymerization. *Mathematical Modelling of Natural Phenomena* **2019**. https://doi.org/10.1051/mmnp/2019059.

(39) Yourdkhani, M. et al. Thermo-Mechanical Properties of Thermoset Polymers and Composites Fabricated by Frontal Polymerization. In *Thakre, P., Singh, R., Slipher, G. (eds) Mechanics of Composite, Hybrid and Multifunctional Materials*; Conference Proceedings of the Society for Experimental Mechanics Series; Springer, 2019; Vol. Volume 5.

(40) Maksimov, Y. M. *Comb. Expl. Shock Waves* **1979**, *15*, 415–418.

(41) Lloyd, E. M.; Feinberg, E. C.; Gao, Y.; Peterson, S. R.; Soman, B.; Hemmer, J.; Dean, L. M.; Wu, Q.; Geubelle, P. H.; Sottos, N. R.; Moore, J. S. Spontaneous Patterning during Frontal Polymerization. *ACS Cent. Sci.* **2021**, *7* (4), 603–612. https://doi.org/10.1021/acscentsci.1c00110.

(42) Pojman, J. A.; Masere, J.; Petretto, E.; Rustici, M.; Huh, D.-S.; Kim, M. S.; Volpert, V. The Effect of Reactor Geometry on Frontal Polymerization Spin Modes. *Chaos* **2002**, *12* (1), 56–65. https://doi.org/10.1063/1.1445436.

(43) Ilyashenko, V. M.; Pojman, J. A. Single-Head Spin Modes in Frontal Polymerization. *Chaos* **1998**, *8* (1), 285–289. https://doi.org/10.1063/1.166308.

Chapter 2: Controllable Frontal Polymerization and Spontaneous Patterning Enabled by Phase-Changing Particles[1]

Frontal polymerization provides a rapid, economic, and environmentally friendly methodology to manufacture thermoset polymers and composites. Despite its efficiency and reduced environmental impact, the manufacturing method is underutilized due to the limited fundamental understanding of its dynamic control. This chapter reports the control and patterning of the front propagation in a dicyclopentadiene resin by immersion of phase-changing polycaprolactone particles. Predictive and designed patterning was enabled by multiphysical numerical analyses, which revealed that the interplay between endothermic phase transition, exothermic chemical reaction, and heat exchange govern the temperature, velocity, and propagation path of the front via two different interaction regimes. To pattern the front, one can vary the size and spacing between the particles and increase the number of propagating fronts, resulting in tunable physical patterns formed due to front separation and merging near the particles. Both single- and double-frontal polymerization experiments in an open mold are performed. The results confirm the front-particle interaction mechanisms and the shapes of the patterns explored numerically. The present study offers a fundamental understanding of frontal polymerization in the presence of heat-absorbing second-phase materials and proposes a potential one-step manufacturing method for precisely patterned polymeric and composite materials without masks, molds, or printers.

[1]This chapter was published in *Small* **2021**, *17*.

2.1 Introduction

Thermoset polymers and composites are integral to the next generation of lightweight, energy-efficient structures due to their excellent specific stiffness and strength, thermal stability, and chemical resistance.[1] While the traditional autoclave-based curing techniques involving elevated temperature and complex pressure cycles are both time- and energy-consuming,[2] a recently introduced manufacturing methodology based on frontal polymerization (FP)[3] employing a self-propagating exothermic polymerization wave triggered by a local thermal stimulus offers a rapid, energy-efficient, and environmentally friendly alternative.[4]

However, FP has so far been limited to fabricating homogeneous polymeric parts without secondary procedures such as etching,[5] deposition,[6] layer-by-layer assembly,[7] or the introduction of a second phase.[8] One-step manufacturing of parts with visible patterns and spatially dependent material properties rely on dynamically controlling the polymerizing front. For example, the sharp variation in front temperature can spontaneously introduce mechanical, chemical, morphological and chemical patterns in the polymer.[9] In FP, many factors affect the velocity and temperature of the polymerization front, and thereby the morphology and properties of the manufactured polymeric and composite part,[10] including the cure kinetics[11] and pre-cure state[12] of the resin, the catalysts and inhibitor concentrations,[10a,11c] the process temperature,[13] pressure,[14] gravity,[15] and the presence of a reinforcing phase.[16] To address this challenge, we present a method for spontaneous control of the thermal energy generated in FP patterning and front propagation using a secondary phase composed of phase-changing materials, which were shown to adjust the front temperature and velocity globally when mixed with the resin in a previous study.[17]

To determine how phase-changing materials would both capture and direct thermal fronts, we combined simulations and experiments - introducing mm-sized polycaprolactone (PCL)

particles with a melting temperature of ~60 °C[18] in a dicyclopentadiene (DCPD) resin. We report how these particles control the temperature and velocity of the front in FP in-situ as the phase transition of the particles partially absorbs the heat released by the polymerization. Through a parametric study of the particle size and the inter-particle distance, two regimes of the front-particle interaction are observed, driven by the competition between the energy and time scale of phase transition, thermal diffusion, and front propagation. The front-particle interactions lead to substantial variations in thermal histories and thermal patterns resulting in controlled pattern formation in the resin. In parallel, FP experiments were conducted, which validate the proposed mechanisms in excellent agreement with the simulations and confirm the correlation between the observed physical patterns and the thermal patterns predicted by numerical analyses. The result of the model and experiment was a predictive system for the generation of patterns via a single phase in polymer composites using FP and phase-changing materials. This system is the key conceptual step in generating patterned composites outside an autoclave and with the other fabrication benefits of FP.

2.2 Frontal polymerization with phase-changing particles results in frontal delay and higher front temperatures

2.2.1 Results and discussion

To understand the interaction between particles and FP for patterning, we conducted parallel experimental and numerical analyses. As the numerical analysis revealed many unexpected results later reflected in the experimental outcomes, we present the numerical analysis first in an attempt to better explain the system before showing the experimental results.

Numerically, the frontal polymerization of DCPD with PCL particles can be captured by seeking transient solutions to the multiphysical reaction-phase-transition-diffusion governing partial differential equations (see Computational Methods) in a numerical domain depicted in Figure 1a. The length l of the 2-D domain is set as 20 mm while the width w is set between 1 to 6 mm to study the effect of the particle size and inter-particle distance. The FP is triggered along the left boundary ($x = 0$), as indicated by the yellow arrows. The front achieves steady-state propagation[19] prior to its interaction with the PCL particle located at $x = 10$ mm and $y = 0$, with a radius r ranging from 0.5 to 2.5 mm. Adiabatic conditions are applied along all boundaries, with these conditions adopted along the lower ($y = 10$) and upper ($y = w$) boundaries of the domain to model the interaction of a polymerization front with an infinite row of melting particles separated by $2w$.

As the front moves around a particle, it experiences unique thermal transfer depending on the particle's size, the front merging, and the amount of energy absorbed by the particle. Each of these parameters can be used to control the time the front "dwells" on the particle, the temperature after the front merges with itself after splitting around the particle, and the energy lost to the particle. The result is that the material can be patterned by controlling the time and temperature that the curing composite experiences, controlled in turn by the size and placement of the particles. Figure 1b presents fields of the temperature T (left), degree of cure α (right, outside the semi-circle), and degree of melting δ (right, inside the semi-circle) solutions at five instants of a typical interaction between the polymerization front and the row of melting particles. The simulated domain has a width $w = 2.5$ mm, and the radius of the PCL particle is $r = 1$ mm. At $t_1 = 7.5$ s, the polymerization front has not yet reached the row of PCL particles and is straight with a constant front velocity $v = 1.06$ mm/s. The temperature behind the front is $T_{max} = 225.6$ °C.

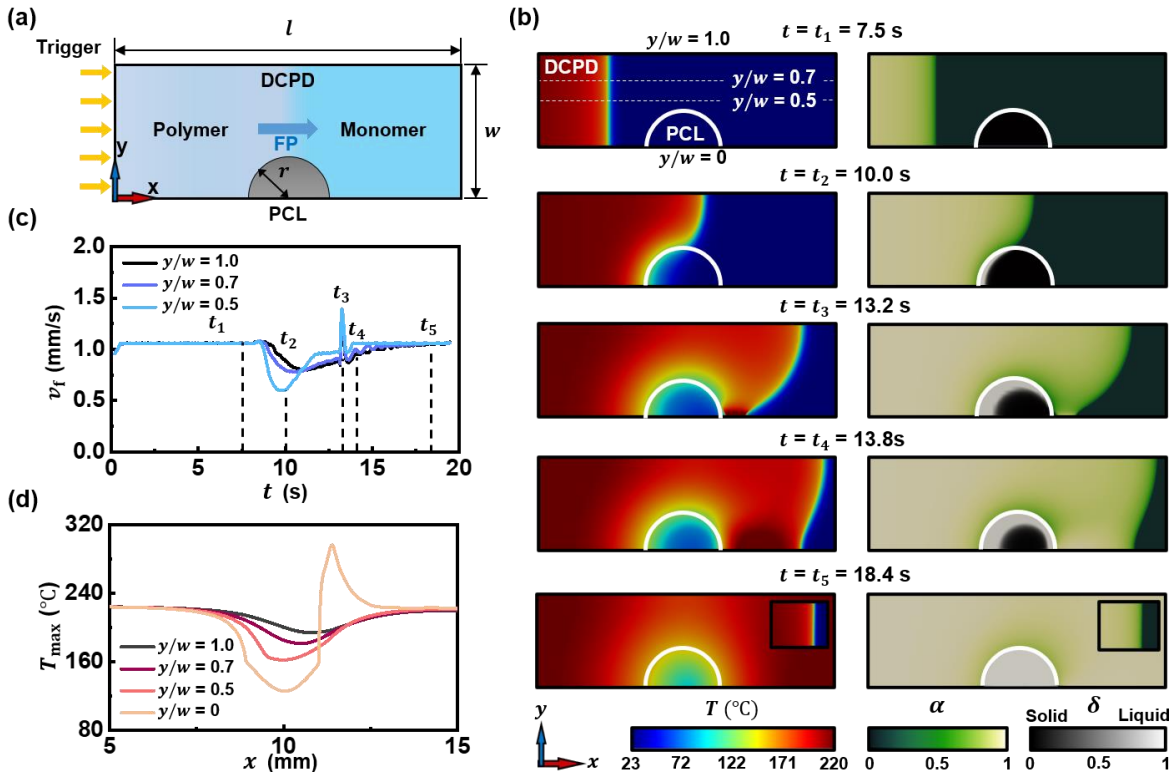

Figure 1. Frontal polymerization of DCPD with PCL particles. a) Problem configuration. A phase-changing particle with a radius of r is centered in the middle of the lower boundary. The frontal polymerization is triggered at the left boundary. Adiabatic boundary conditions are applied at all other boundaries. b) Fields of temperature T (left figures) and fields of degree of cure α and degree of melting δ (right figures) at five instants (t_1 to t_5) during the front/particle interaction. Inset: the front at t_5. c) Evolution of the front velocity v_f and d) spatial profile of maximum temperature T_{max} along different horizontal lines (y / w = 0, 0.5, 0.7, and 1.0).

When the front reaches the particle at t_2 = 10.0 s, the high temperature of the front triggers the melting of the PCL particle, which absorbs heat and reduces the local temperature, damping the polymerizing reaction and reducing the front velocity. As expected, the front velocity v_f is reduced closer to the particle (Figure 1c), leading to the curvature of the front. At $y \leq r$, the front propagation is temporarily arrested by the presence of the particle while the front moves around the particle and reaches the lower edge of the domain behind the particle at t_3 = 13.2 s. The merging fronts circumnavigating the particle along its upper side with its counterpart moving along the lower part

of the particle leads to a thermal spike reaching a temperature of 292.4 ℃, as illustrated in Figure 1d for $y / w = 0$.

The high-temperature thermal spike spreads along with the front profiles and dissipates, leading to a sudden increase in the front velocity v_f, especially in the region just above the particle (curve $y / w = 0.5$ in Figure 1b). At $t_4 = 13.8$ s, the front behind the particle accelerates to catch up with the front at $y / w = 1$ while most of the particle is still in the solid phase. At $t_5 = 18.4$ s, the front travels away from the now fully melted particle and restores its initial velocity of $v_f = 1.06$ mm/s and its vertical shape, as presented in the insets. From this initial model, we determined that the most critical factors were the front temperature and the particle size (r). The observation that local front temperatures can be increased at highly local spots above the initial FP temperature by more than 75 ℃ was important as it demonstrated how this method could localize heating within the material in an organized fashion. We had not yet explored how these parameters could change or if different regimes between heat dissipation and absorption would result in differences in patterning. In the next section, we examined how varying these parameters resulted in different patterning capabilities from different front regimes.

2.2.2 Methods

Computational Methods

Frontal polymerization in the DCPD resin (denoted hereafter by the subscript r) is modeled with the aid of the following reaction-diffusion partial differential equations in terms of the temperature T (in K) and degree of cure α (non-dimensional) fields:[4]

$$\begin{cases} \kappa_{\mathrm{r}}\left(\frac{\partial^2 T}{\partial x^2}+\frac{\partial^2 T}{\partial y^2}\right)+\rho_{\mathrm{r}}H_{\mathrm{r}}\frac{\partial \alpha}{\partial t}=\rho_{\mathrm{r}}C_{p,\mathrm{r}}\frac{\partial T}{\partial t}, \\ \frac{\partial \alpha}{\partial t}=A_{\mathrm{r}}\exp\left(-\frac{E_{\mathrm{r}}}{RT}\right)f(a). \end{cases} \quad (1)$$

In equation (1), κ_{r} (in W/mK) denotes the thermal conductivity of the resin, $C_{p,\mathrm{r}}$ (in J/kg·K) the specific heat, ρ_{r} (in kg/m^3) the density, and H_{r} (in J/kg) the heat generated by the exothermic reaction of the resin. The second equation describes the cure kinetics of DCPD based on the Prout-Tompkins autocatalytic model with diffusion effects, where $f(\alpha)=(1-\alpha)^n\alpha^m\frac{1}{1+\exp\left[c_{\mathrm{d}}(\alpha-\alpha_{\mathrm{d}})\right]}$. A_{r} (in s), E_{r} (in J/mol), and R (8.314 J/mol·K) respectively denote the pre-exponential factor, activation energy, and ideal gas constant. n and m correspond to the reaction order, while c_{d} and α_{d} describe the particle diffusion control regime of the reaction at higher values of the degree of cure.[20]

Similarly, the solution for the PCL particle (denoted by the subscript p) is described by the following 2-D melting-diffusion partial differential equation written in terms of the thermal field and the degree of melting δ (non-dimensional):

$$\begin{cases} \kappa_{\mathrm{p}}\left(\frac{\partial^2 T}{\partial x^2}+\frac{\partial^2 T}{\partial y^2}\right)-\rho_{\mathrm{p}}H_{\mathrm{p}}\frac{\partial \delta}{\partial t}=\rho_{\mathrm{p}}C_{p,\mathrm{p}}\frac{\partial T}{\partial t}, \\ \frac{\partial \delta}{\partial t}=A_{\mathrm{p}}\exp\left(-\frac{E_{\mathrm{p}}}{RT}\right)g(\delta). \end{cases} \quad (2)$$

In Equation 2, H_{p} denotes the melting enthalpy and the negative sign indicates the endothermic nature of the melting process. The second equation approximates the melting of the PCL particle as a first-order kinetic model, where $g(\delta) = (1 - \delta)$. A_{p} and E_{p} stand for the pre-exponential constant and the activation energy of the melting, respectively.[18] The material properties and the parameters entered in the cure and melting kinetics models used in the present study are summarized in Table

1 and 2, respectively. When compared with experiments, an additional heat loss term $-H_{loss} \cdot (T - T_0)$ is added to the left-hand-side of the first equation in Equation 1 and 2, where H_{loss} = 24.5 kW/m^3 is the heat loss coefficient and is determined by fitting the local temperature history in experiments (Figure A9 in Appendix A). According to the differential scanning calorimetry (DSC) measurements (Figure A10), the melting enthalpy H_p is set as 80 J/g for comparison with experiment (Figure 5 and 6) and is set as 139 J/g, the theoretical value of fully crystalline PCL,[21] in Figures 1-4.

Table 1. Thermal conductivity, density, heat capacity, and thermal diffusivity of DCPD and PCL.

	κ (W/mK)	ρ (kg/m^3)	C_p (kg/m^3)	D (m^2/s)
DCPD (r)	0.15	980	1600.0	9.69×10^{-8}
PCL (p)	0.14	1145	1409.5	8.67×10^{-8}

Table 2. Parameters defining the cure kinetic model in Equation 1 of DCPD and the melting kinetic model in Equation 2 of PCL.

	A (1/s)	E (J/mol)	H (J/kg)	n	m	c_d	α_d
DCPD (r)	8.55×10^{15}	110,750	350,000	1.72	0.77	14.48	0.41
PCL (p)	4.94×10^{35}	241,000	139,000	-	-	-	-

To solve these governing PDEs in both sub-domains, we adopt the following initial and boundary conditions:

$$\begin{cases} T(x,y,0) = T_0, \\ \alpha(x,y,0) = \alpha_0, \text{(in DCPD)} \\ \delta(x,y,0) = \delta_0, \text{(in PCL)} \\ T(0,y,t) = T_{trig}, 0 \le t \le t_{trig}, \\ \frac{\partial T}{\partial x}(0,y,t) = 0, t > t_{trig}, \end{cases} \quad (3)$$

where T_0 (23 °C), α_0 (0.074), δ_0 (0.01), T_{trig} (200 °C), and t_{trig} (1 s) respectively denote the initial temperature, the initial degree of cure, the initial degree of melting, the triggering temperature, and the triggering time. The initial degree of cure α_0 = 0.07 is adopted to simulate the gelled resin. Adiabatic boundary conditions are applied along the other boundaries.

The Multiphysics Object-Oriented Simulation Environment (MOOSE), an open-source C++ finite element solver that includes the robust mesh adaptivity needed to capture the sharp gradients in the vicinity of the moving front, is adopted in this study.

The position of the polymerization front and the boundary separating the solid and liquid phases in the PCL particles are denoted by the locations where α = 0.5 and δ = 0.5, respectively. The reference temperature T_{ref} used in the normalization of the thermal solution is the temperature present behind the polymerization front in the absence of PCL particles:

$$T_{\text{ref}} = T_0 + (1 - \alpha_0) \cdot H_{\text{r}} / C_{\text{p,r}} = 225.6 \text{ °C}. \quad (4)$$

To describe the progress of FP during the front-particle interaction, the relative location of the front is defined as $\widehat{x_f}$ = (x_{f} - $x_{\text{pcl,left}}$) / 2r, where x_{f} and $x_{\text{pcl,left}}$ respectively denote the x-

coordinates of the front (α = 0.5) at y / w = 1 and the left boundary of the PCL. The front temperature, T_f, is defined as the instantaneous local temperature in the resin at the time of the passage of the front, i.e., $T_f = T_{@\alpha=0.5}$.

Experimental Methods

Materials: Dicyclopentadiene (DCPD), 5-ethylidene-2-norbornene (ENB), second-generation Grubbs' catalyst (GC2), phenylcyclohexane, and tributyl phosphite (TBP) inhibitor were purchased from Sigma-Aldrich and used as received without further purification. Polycaprolactone (PCL, MW 43,000) pellets were purchased from Polysciences.

Resin preparation: Given that DCPD is solid at room temperature, it is first melted at 35 ℃ and mixed with 5 wt% ENB to depress the melting point. All references to DCPD herein refer to this 95/5 DCPD/ENB solution. This mixture is then degassed at 28 kPa overnight. In a typical experiment, 3.21 mg GC2 is weighed out into an Eppendorf tube and dissolved in 400 μL phenylcyclohexane. One molar equivalent of TBP inhibitor with respect to GC2 is added to the solution via a volumetric syringe. The catalyst/inhibitor solution is then added to 5 g of DCPD (10,000 molar equivalents with respect to GC2) and thoroughly mixed with vortex for 1 min and then put in a sonic bath for 20 min.

PCL cylindrical particle fabrication: Following complete melting of the PCL pellets at 120 ℃, a pre-heated syringe is used to inject the molten PCL into a pre-heated polytetrafluoroethylene (PTFE) tubing with 5 mm inner diameter. The PCL is allowed to solidify at room temperature. It is then removed from the tubing and cut into 5 mm sections, yielding cylinders with 5 mm height and diameter.

Frontal polymerization: FP experiments are conducted in a rectangular mold. The length of the mold (in the FP direction) is 120 mm. The width of the mold (perpendicular to the FP direction) is set between 37 and 45 mm and is determined by the desired spacing 2*w* between PCL cylinders as 2*nw*-(2*w*-2*r*), where n is the number of cylinders chosen. A FLIR E8 Thermal Imaging Camera is adopted to monitor the temperature evolution. A photo of the setup is given in Figure A4 in the Appendix A. For single-front experiments, cylinders are placed 30 mm from the opposite ends where frontal polymerization is initiated to allow sufficient space for the front to achieve steady-state conditions. With two fronts initiated at opposite ends, the two rows of cylinders are placed equidistant from the center of the mold. To suppress the convective motion of the resin during FP, after placing the cylinders in the mold, the DCPD solution is poured in and allowed to polymerize for 4 h at room temperature to create a gel. One (or two) soldering iron(s) is(are) used to initiate the frontal ring-opening metathesis polymerization (FROMP) reaction.

Confocal microscope scanning: The volume containing the optically visible patterns at the surface was full-thickness imaged using the RS-G4 ribbon scanning, upright confocal microscope (Caliber I.D.). The data were in the reflection mode, taken using the 785 nm laser. 8 kHz scan rate, 1024 pixel lines, tiled images were collected and stitched via acquisition software. The objective was Olympus 10X NA 0.3 dry (UPlanFL). Pixel output size was 1.289 μm. Laser power was adjusted to fill most of the 16-bit photomultiplier detector range. Images were viewed and analyzed using Arivis Vision4D software v. 3.1.

2.3 Two regimes of front-particle interactions guided by energy competition result in distinct front design space

2.3.1 Results and discussion

The propagation and trajectories of a polymerization front can be controlled by the radius r of the PCL particles and the spacing $2w$ between these particles. This control is a result of the energy competition between the exothermic FP, the endothermic phase transformation, and the thermal diffusion, leading to two front-particle interaction regimes dominated by different physics. Each regime provides a different tool for controlling the front by shaping the contour temperature of the front. Figure 2a-c respectively illustrate Regime I, Regime II-a, and Regime II-b. To identify the leading physics in each regime, the progress of FP and phase transformation are reflected by the relative location of the front $\widehat{x_{\mathrm{f}}}$ (see Computational Methods) and the average degree of melting in the particle $\bar{\delta}$, respectively. The contour of front temperature T_{f} is presented to reflect the result of energy competition and denote the front trajectory with arrows in each regime.

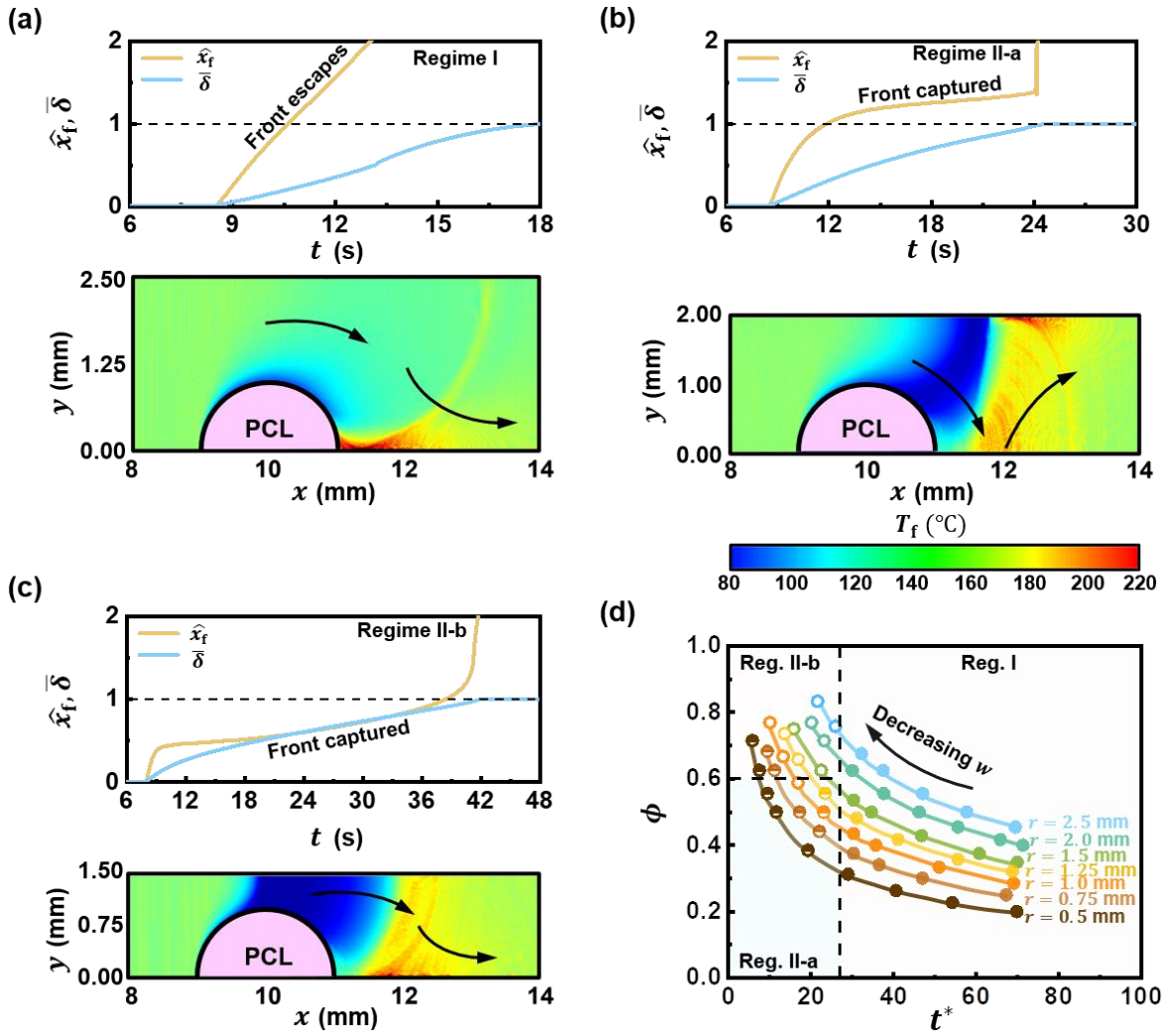

Figure 2. Physical mechanisms in different regimes of front-particle interactions. Time evolution of the front position $\hat{x}_f$ and average degree of melting in the particle $\bar{\delta}$, and front temperature contours T_f in a) Regime I, b) Regime II-a, and c) Regime II-b. d) Regime design space in the plane of characteristic time length ratio $t^* = t_{MD} / t_{FP}$ and particle line fraction $\phi = r / w$. The solid, half-filled, and hollow circles indicate Regimes I, II-a, and II-b, respectively.

Regime I - reduced frontal velocity and thermal spikes. In Regime I, the combination of r = 1 mm and w = 2.5 mm shown in Figure 1a results in a front that escapes from the cooling effect associated with the phase transition and leaves the particle $\hat{x}_f$ = 1 with less than 25% of the melting completed, indicating the leading physics is FP. The same phenomenon is also reflected in the T_f distribution, where the temperature drop (blue contours) is limited to a small region adjacent to the

particle and causes a slight reduction in the front velocity (Figure A1 in Appendix A). Indicated by the black arrows, the merging of fronts behind the particle leads to a thermal spike in a small range (Movie S1). These results suggest that Regime I is suitable for achieving a slight velocity variation and a thermal spike with a small area.

Regime II-a - temporary front capture with melting. By keeping r = 1 mm but reducing the particle half-spacing to w = 2 mm, we observed a new design space which enhanced the cooling effect of the phase transition from Regime II-a. The front is temporarily captured behind the particle due to a considerable reduction in its velocity as reflected by the evolution of $\hat{x}_{\mathrm{f}}$, and resumed propagation after the melting was complete ($\bar{\delta}$ = 1), suggesting the leading physics is melting and thermal diffusion. Correspondingly, a notable reduction in T_{f} (a broad blue region in Figure 2b) is observed. The front trajectory is different from Regime I due to the interaction as shown by the arrows, leading to a thermal spike with a large area (Movie S2). These observations demonstrate that Regime II-a may be used to delay front propagation and to generate a thermal spike with a large area.

Regime II-b - full front capture by melting. By decreasing w to 1.5 mm, the cooling effects are further enhanced in Regime II-b presented in Figure 2c. As in Regime II-a, the front is captured during the energy competition as indicated by the time evolution of $\hat{x}_{\mathrm{f}}$, and resumes propagation when the melting process is almost complete. A significant reduction in T_{f} is observed in a wider range compared to Regime II-a, resulting in a different front trajectory and a wide range of thermal spike (Movie S3). These analyses suggest that Regime II-b can be used to induce a front velocity reduction and a larger region of thermal spike allowing greater patterning opportunities.

After examining the individual regimes, we determined that by combining them into pairs and sets using quantitative analysis of r and w (Figure 2d), one could develop unique design spaces

for the line fraction of the particles $\phi = r / w$ (vertical axis), which accounts for the relevant dimensions and the melting diffusion-to-FP characteristic time ratio $t^* = t_{MD} / t_{FP}$ (horizontal axis). The FP time-scale is defined as $t_{FP} = 2r / v_\infty$, where $v_\infty = 1.06$ mm/s is the front velocity in the absence of the particle. The melting diffusion time scale is defined as $t_{MD} = w^2 / \overline{D}$, where $\overline{D} = [D_p \cdot r + D_r \cdot (w - r)] / w$ is an effective thermal diffusivity of the composite material. In the map presented in Figure 2d, the solid, half-filled, and hollow circles denote Regimes I, II-a, and II-b, respectively. More discussion about the design space can be found in Figure A2 in Appendix A. With these unique design tools in hand, we conjectured that it would be possible to use interacting fronts to shape new patterns within a composite material using patterned phase change materials to selectively alter the shape of fronts in a controlled fashion. However, we still needed to assemble combined models which could enable predictive patterns of thermal energy by combining all the regimes into a single model.

2.4 Front velocities and thermal patterns during front-particle interactions

2.4.1 Results and discussion

To begin building a model for designing thermal patterning of composite materials, we sought to define the control of front velocity in different regimes, using an average `interaction velocity' of the front defined as $v_{int} = x_{int} / t_{int}$, where x_{int} and t_{int} respectively denote the front propagation distance and time during the front-particle interaction (Figure A3). Figure 3 illustrates the dependence of v_{int} normalized by v_∞ on the time ratio t^* (Figure 3a) and on the particle line fraction ϕ (Figure 3b). Both figures show a clear break between the solutions associated with Regime I and those corresponding to Regime II. As expected, for large values of t^*, the front

velocity is hardly impacted by the particles, leading to v_{int} / v_∞ increasingly approaching unity following a general trend that regroups all values of the particle radius considered in this study. For values of t^* less than the aforementioned value of 27 corresponding to Regime II, the increasing influence of the heat absorbed by the melting particles leads to a significant delay of the forward motion of the front. Defining these interactions allowed us to determine when materials would experience different regimes.

Figure 3b points to the existence of a similar general trend in the (v_{int}, ϕ) plane for Regime II, for which the duration of the front-particle interaction dominates v_{int}. Larger values of ϕ correspond to longer durations of the front-particle interaction and thereby to decreasing values of v_{int}.

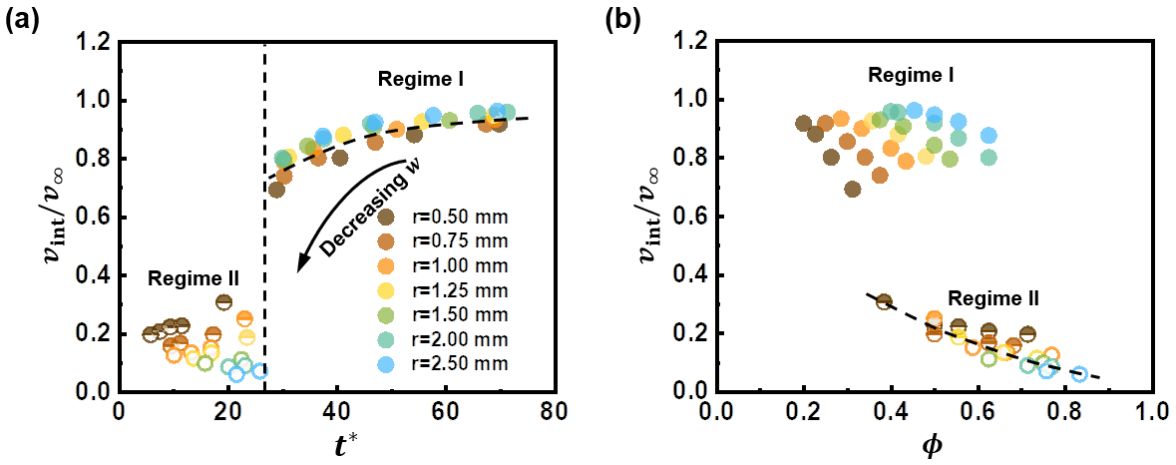

Figure 3. Average front velocity v_{int} during the front-particle interaction event normalized by the front velocity in the absence of the particle v_∞ as a function of a) the characteristic time ratio t^* and b) the particle line fraction ϕ.

As shown earlier in Figure 1 b-d, the front merging taking place behind the PCL particles can generate a localized temperature rise that exceeds the maximum temperature T_{ref} associated with the front in neat DCPD. The heterogeneous distribution of the maximum temperature experienced by the DCPD resin during FP could be used to generate patterns in the manufactured part and to

spatially organize material properties. Figure 4a shows the correlation between the maximum temperature during the front-particle interaction T_{max} (absolute temperature, in K) divided by the reference temperature T_{ref} (absolute temperature, in K) and the characteristic time ratio t^*, which further depends on the geometry of the system. For the system in Regime I (solid circles), the front temperature T_f before the merging (150 °C) is barely affected (Figure 2a), leading to a value of T_{max} that is independent of w at a specific r. However, when $t^* < 27$ (Regime II-a, half-filled circles, and Regime II-b, hollow circles), a decreasing trend of T_{max} with the decrease of w can be observed, which is caused by a lower T_f before the merging due to more adequate front-particle interactions (Figure 2a-c).

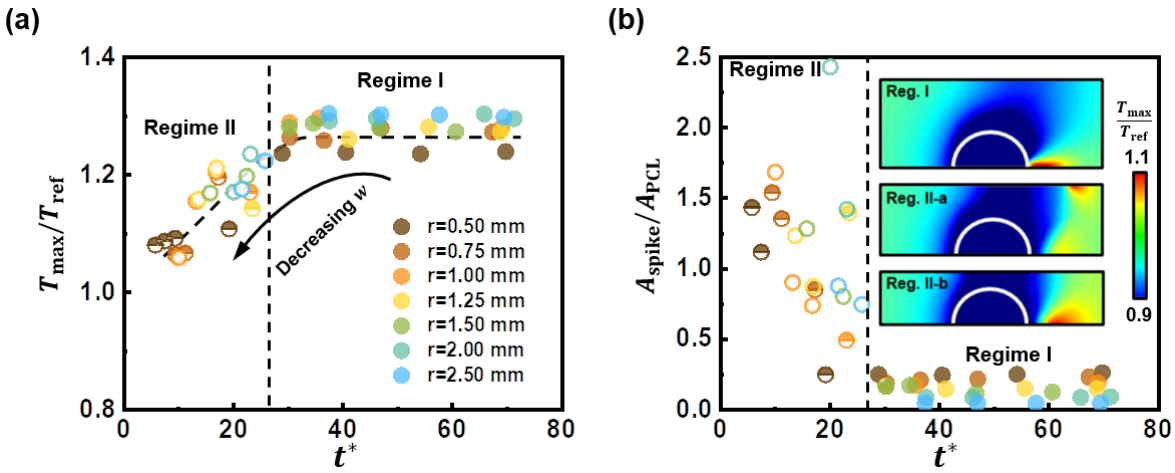

Figure 4. a) Maximum temperature T_{max} (normalized by the temperature of the front in the absence of particles) experienced by the DCPD resin as a function of the characteristic time ratio t^*. b) Normalized thermal spike area of A_{spike} / A_{PCL} versus the characteristic time length t^*. Inset: fields of local maximum temperature T_{max} normalized by the maximum temperature in the neat resin T_{ref}.

Figure 4b presents the area of the thermal spike A_{spike} for which $T_{max} / T_{ref} > 1.01$ (both in K). A_{spike} is normalized by the area of the half-particle $A_{PCL} = 0.5 \cdot \pi r^2$ to compare the systems with different particle sizes. For the systems in Regime I (solid circles), A_{spike} / A_{PCL} is independent of t^*. However, for a specific value of r, reducing w for Regime II (half-filled and hollow circles) results

in a significant increase of A_{spike} / A_{PCL}, as also reflected by the inset fields of T_{max} / T_{ref} (both in K). The higher values of T_{max} / T_{ref} associated with Regime II are caused by the higher front temperature T_f obtained after the fronts merge (Figure 2a-c). Using the relationship between front temperature and time, we can predict a desired pattern and front velocity based on the size and spacing of particles.

2.5 Experimental validation of predictive patterning via frontal polymerization with phase-changing particles

2.5.1 Results and discussion

To validate the numerical result, a set of FP experiments involving PCL cylindrical particles immersed in DCPD were conducted in parallel. The experimental setup consisting of a rectangular open mold and a set of PCL cylindrical particles is similar to that adopted in simulations (Figure 1a) and is depicted in Figure A4 in Appendix A. All experiments were performed at room temperature (~23 °C). Figure 5a presents experimental snapshots of the interaction between the polymerization front and the PCL particles. The adopted particle radius and half-particle spacing are chosen to be r = 2.5 mm and w = 5 mm, respectively. The observed evolution of the front shape (Movie S4) is consistent with the simulated evolution obtained with the same values of r and w and conducted by solving the reaction-phase-transition-diffusion PDEs that include an additional convection heat loss term (Computational Methods) to capture approximately the heat loss to the surroundings. The introduction of the convective heat loss term reduces the simulated front velocity v_∞ to 1.04 mm/s, in good agreement with the measured value of 1.03 ± 0.03 mm/s.

Figure 5b presents the dependence of the normalized 'interaction front velocity' v_{int} / v_{∞} on the line fraction of the particle ϕ, showing good agreement between numerical and experimental results. The method used to extract v_{int} and v_{∞} in the experiments is described in Figure A5 in Appendix A. A decreasing v_{int} / v_{∞} can be achieved by increasing ϕ, consistent with the results shown in Figure 3a. However, Regime II is not observed in the experiments: when ϕ exceeds 0.7, the front is quenched (Movie S5) by the convective heat loss (i.e., $v_{int} / v_{\infty} = 0$), as also shown in the simulations (Figure A6). Figure 5c presents a close-up picture of the sample with r = 2.5 mm and w = 3.75 mm after FP, showing a pattern behind each particle generated by the thermal spike created by the front merging. Again, the shape of the thermal patterns is consistent with that of the thermal spike predicted numerically (Figure 5d).

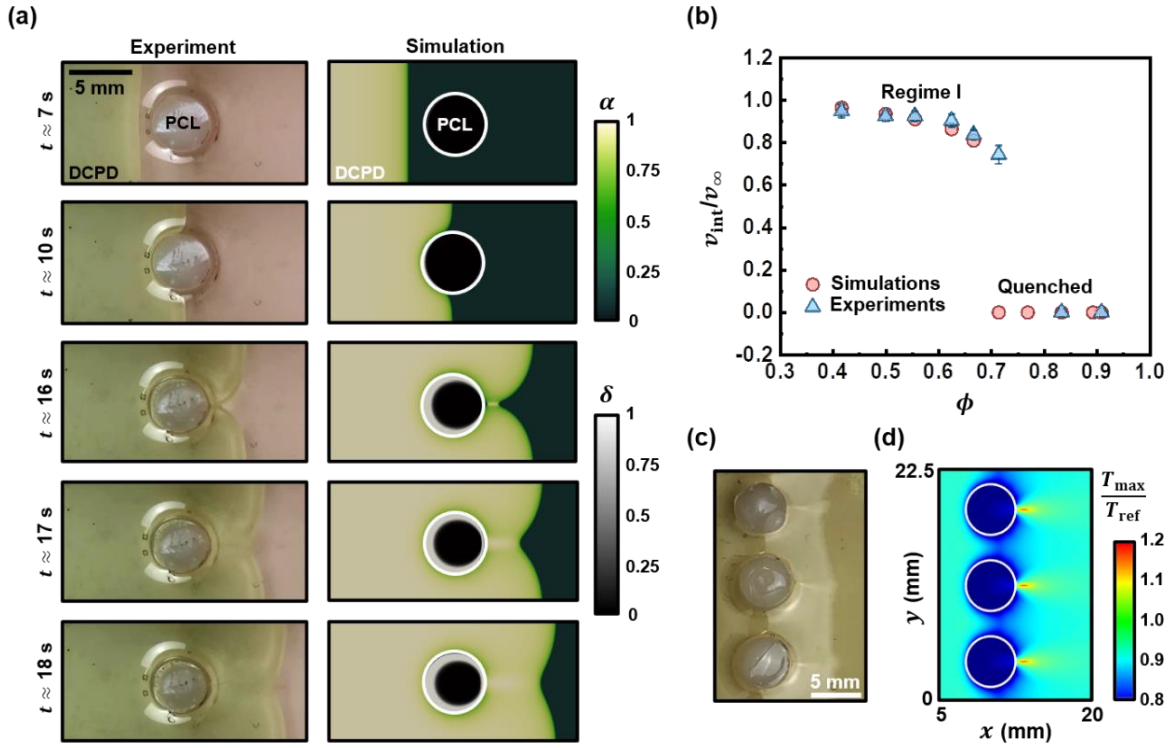

Figure 5. a) Comparison between experimentally observed and numerically predicted interaction between the polymerization front and the row of PCL particles with r = 2.5 mm and w = 5 mm. b) Dependence of the observed and predicted interaction velocity v_{int} / v_∞ on the particle line fraction ϕ. In this plot, v_∞ is 1.04 and 1.03 mm/s in simulations and experiments, respectively. c) Details on the DCPD/PCL system with r = 2.5 mm and w = 3.75 mm after FP. d) Predicted thermal pattern for the case shown in c).

A wide variety of thermal patterns can be predicted and then generated by designating how two converging, propagating fronts interact with two rows of PCL particles as they merge in the middle of the domain (Figure 6a). The dimensions of the simulated domain are given by l = 20 mm, r = 1 mm, and w = 2.5 mm, leading to Regime I (Figure 2a). The two rows of particles are set symmetrically from the middle line (x = 10 mm) at a distance ranging from 2 to 6 mm. Details of the interaction between the two polymerization fronts and the particles and the associated thermal patterns are provided in Figure 6b when the gap between the two rows of particles is 4 mm. As apparent in the two snapshots obtained at time t = 10.1 s and 10.2 s, front merging takes place at three thermal spike locations marked by the arrows (Movie S6).

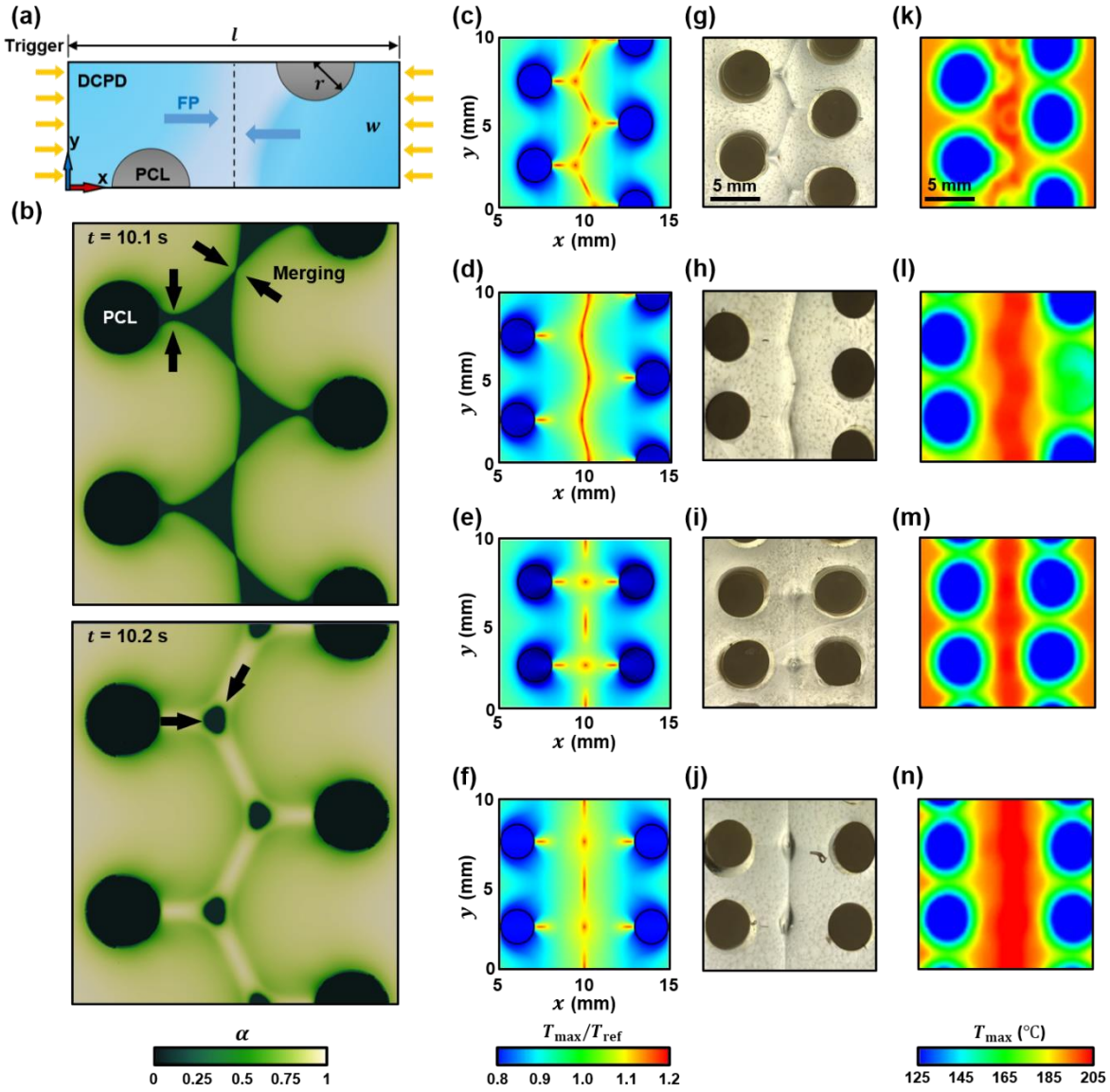

Figure 6. Thermal patterns achieved through the interaction of converging fronts with two parallel rows of PCL particles. a) Schematic description of the numerical model. b) Front merging process, with the arrows pointing to the location of the thermal spikes. c-f) Thermal patterns achieved by adjusting the relative locations of the particles and the inter-particle distance. g-j) Observed physical patterns, showing good agreement with the numerical predictions. k-n) Experimental IR thermal patterns.

Most notably, the thermal pattern can be predicted and designed by the relative position of the particles, as illustrated in Figure 6c-f and Figure A7 in Appendix A. To validate these numerical

results, multi-front FP experiments in DCPD with two rows of PCL particles are conducted (Movie S7). The fronts lead to visible patterns as they merge, and the shapes of the patterns are consistent with the simulated thermal histories (Figure 6g-j). Figure 6k-n present the maximum temperature T_{max} contours obtained with an IR camera, which partially capture the shape of thermal spikes (high temperature in the middle). The design space of thermal patterns can be further enlarged by breaking the symmetry of the problem and adopting a difference in distance between the front initiation and the rows of particles (Figure A7). Confocal microscopy scanning reveals that the patterns persist from the surface through the thickness of the polymerized sample, influencing adjacent microstructures (Figure A8).

2.6 Conclusions

In summary, through numerical analysis and experiments, we demonstrated that the frontal polymerization of DCPD can be effectively predicted and controlled by introducing melting PCL particles in the resin. By varying the size and spacing of the PCL particles, different regimes of front-particle interaction can be formed due to the competition between frontal polymerization, particle melting, and thermal diffusion. This interaction leads to predictable and adjustable front velocities and thermal patterns in the frontally polymerized matrix. We captured the key features of these interactions in FP experiments in an open mold containing cylindrical PCL particles embedded in a layer of DCPD monomer, including the relation between the front velocity and the particle spacing. Using this fundamental understanding, we establish that propagating fronts can be used to design patterns in composite materials using two parallel rows of PCL particles that interact with two converging fronts. The control of FP through the insertion of heat-absorbing phase-changing particles demonstrates a potential approach for predictive, design-guided FP-

based manufacturing of polymer materials with temperature-dependent patterns and material properties.

2.7 References

(1) a) J. P. Pascault, H. Sautereau, J. Verdu, R. J. Williams, *Thermosetting Polymers*, Vol. 64, CRC Press, FL, USA, **2002**; b) P. Brondsted, H. Lilholt, A. Lystrup, *Annu. Rev. Mater. Res.* **2005**, *35*, 505; c) V. M. Karbhari, F. Seible, *J. Appl. Compos. Mater.* **2000**, *7*, 95; d) I. M. Daniel, O. Ishai, I. M. Daniel, I. Daniel, *Engineering Mechanics of Composite Materials*, Vol. 3, Oxford University Press, NY, USA, **1994**.

(2) a) D. Abliz, Y. Duan, L. Steuernagel, L. Xie, D. Li, G. Ziegmann, *Polym. Polym. Compos.* **2013**, *21*, 341; b) A. J. Timmis, A. Hodzic, L. Koh, M. Bonner, C. Soutis, A. W. Schäfer, L. Dray, *Int. J. Life Cycle Ass.* **2015**, *20*, 233.

(3) a) J. A. Pojman, G. Curtis, V. M. Ilyashenko, *J. Am. Chem. Soc.* **1996**, *118*, 3783; b) D. I. Fortenberry, J. A. Pojman, *J. Polym. Sci., Part A: Polym. Chem.* **2000**, *38*, 1129; c) A. Mariani, S. Fiori, Y. Chekanov, J. A. Pojman, *Macromolecules* **2001**, *34*, 6539; d) S. Davtyan, A. Berlin, A. Tonoyan, *Rev. J. Chem.* **2011**, *1*, 56; e) S. Fiori, A. Mariani, L. Ricco, S. Russo, *e-Polym.* **2002**, *2*; f) A. Ruiu, D. Sanna, V. Alzari, D. Nuvoli, A. Mariani, *J. Polym. Sci., Part A: Polym. Chem.* **2014**, *52*, 2776.

(4) I. D. Robertson, M. Yourdkhani, P. J. Centellas, J. E. Aw, D. G. Ivanoff, E. Goli, E. M. Lloyd, L. M. Dean, N. R. Sottos, P. H. Geubelle, J. S. Moore, S. R. White, *Nature* **2018**, *557*, 223.

(5) D. L. Flamm, O. Auciello, *Plasma deposition, treatment, and etching of polymers: the treatment and etching of polymers*, Elsevier, Amsterdam, Netherlands, **2012**.

(6) A. Malinauskas, *Polymer* **2001**, *42*, 3957.

(7) J. J. Richardson, J. Cui, M. Björnmalm, J. A. Braunger, H. Ejima, F. Caruso, *Chem. Rev.* **2016**, *116*, 14828.

(8) a) V. Alzari, D. Nuvoli, S. Scognamillo, M. Piccinini, E. Gioffredi, G. Malucelli, S. Marceddu, M. Sechi, V. Sanna, A. Mariani, *J. Mater. Chem.* **2011**, *21*, 8727; b) D. Nuvoli, V. Alzari, J. A. Pojman, V. Sanna, A. Ruiu, D. Sanna, G. Malucelli, A. Mariani, *ACS Appl. Mater. Interfaces* **2015**, *7*, 3600.

(9) E. M. Lloyd, E. C. Feinberg, Y. Gao, S. R. Peterson, B. Soman, J. Hemmer, L. M. Dean, Q. Wu, P. H. Geubelle, N. R. Sottos, *ACS Cent. Sci.* **2021**, *7*, 603.

(10) a) I. D. Robertson, E. L. Pruitt, J. S. Moore, *ACS Macro Lett.* **2016**, *5*, 593; b) Y. A. Chekanov, J. A. Pojman, *J. Appl. Polym. Sci.* **2000**, *78*, 2398.

(11) a) H. Liu, H. Wei, J. S. Moore, *ACS Macro Lett.* **2019**, *8*, 846; b) A. Mariani, S. Bidali, S. Fiori, M. Sangermano, G. Malucelli, R. Bongiovanni, A. Priola, *J. Polym. Sci., Part A: Polym. Chem.* **2004**, *42*, 2066; c) S. Chen, Y. Tian, L. Chen, T. Hu, *Chem. Mater.* **2006**, *18*, 2159.

(12) E. Goli, I. D. Robertson, P. H. Geubelle, J. S. Moore, *J. Phys. Chem. B* **2018**, *122*, 4583.

(13) N. Gill, J. A. Pojman, J. Willis, J. B. Whitehead Jr, *J. Polym. Sci., Part A: Polym. Chem.* **2003**, *41*, 204.

(14) C. Nason, T. Roper, C. Hoyle, J. A. J. M. Pojman, **2005**, *38*, 5506.

(15) W. J. Ainsworth, J. A. Pojman, Y. A. Chekanov, J. Masere, ACS Publications, DC, USA, 2001.

(16) a) S. Vyas, X. Zhang, E. Goli, P. Geubelle, *Compos. Sci. Technol.* **2020**, 108303; b) E. Goli, N. Parikh, M. Yourdkhani, N. Hibbard, J. Moore, N. Sottos, P. Geubelle, *Composites, Part A* **2020**, *130*, 105689.

(17) V. G. Viner, J. A. Pojman, D. Golovaty, *Phys. D: Nonlinear Phenom.* **2010**, *239*, 838.

(18) F. Fraga-López, J. Manuel Martínez-Ageitos, E. Rodríguez-Núñez, J. Blanco-Mendez, A. Luzardo-Álvarez, E. Calvo-Carnota, L. Jiménez-Carrillo, *J. Appl. Polym. Sci.* **2011**, *121*, 3635.

(19) S. Vyas, E. Goli, X. Zhang, P. H. Geubelle, *Compos. Sci. Technol.* **2019**, *184*, 107832.

(20) G. Yang, J. K. Lee, *Ind. Eng. Chem. Res.* **2014**, *53*, 3001.

(21) M. A. Woodruff, D. W. Hutmacher, *Prog. Polym. Sci.* **2010**, *35*, 1217.

Chapter 3. Manipulating Frontal Polymerization and Instabilities with Phase-Changing Microparticles[2]

Recently presented as a rapid and eco-friendly manufacturing method for thermoset polymers and composites, frontal polymerization (FP) experiences thermo-chemical instabilities under certain conditions, leading to visible patterns and spatially dependent material properties. In the previous chapter, we presented a predictive approach to FP-based manufacturing of patterned materials using discrete macro-particles of a phase-change material in dicyclopentadiene (DCPD). Through numerical analyses and experiments, in this chapter we demonstrate how the front velocity, temperature, and instability in the frontal polymerization of cyclooctadiene, an additional FP monomer of interest, are affected by the presence of poly(caprolactone) microparticles homogeneously mixed with the resin. The phase transformation associated with the melting of the microparticles absorbs some of the exothermic reaction energy generated by the FP, reduces the amplitude and order of the thermal instabilities, and suppresses the front velocity and temperatures. Experimental measurements validate predictions of the dependence of the front velocity and temperature on the microparticle volume fraction provided by the proposed homogenized reaction−diffusion model.

3.1 Introduction

[2] This chapter was published in *J. Phys. Chem. B* **2021**, *125,* 27, 7537–7545. First authorship of this work corresponds to Dr. Yuan Gao. It is included in this thesis due to my significant contributions in the conceptualization of the project and the design and execution of the experiments.

Recently introduced as a rapid, energy-efficient, eco-friendly, out-of-autoclave alternative to conventional bulk-polymerization-based manufacturing for thermoset composites,[1] frontal polymerization (FP) is based on the self-sustaining process associated with the propagation of a sharp polymerization front driven by the exothermic reaction taking place in the thermosetting resin.[2-5] The key features of the FP-based manufacturing process, including the front temperature and velocity, are sensitive to many factors, including the formulation of the resin,[6−11] the presence of a thermally conductive reinforcing phase,[12−15] the environmental temperature,[16−18] and pressure.[19,20] All of these factors have been shown to affect the morphology and properties of the resultant polymer.[21−24] In most cases, the polymerization front propagates in a steady fashion, leading to the manufacturing of polymeric materials with homogeneous properties. However, under certain conditions,[25−27] thermo-chemical instabilities are observed in the front propagation, characterized by highly transient front temperatures and velocities. These instabilities have been reported in previous studies as pulsating,[28−30] spinning,[2,31,32] and fingering instabilities.[33] The ultimate objective of this work is to harness these thermal instabilities by changing the process conditions through the tuning of the reaction and thermal transport, leading to spontaneous and controllable patterns and spatially dependent morphological, chemical, optical, and mechanical properties in the polymer.[34] The numerical and experimental study presented hereafter has two main goals: (1) to investigate how the introduction of microparticles with a melting temperature below the front temperature affects the front velocity and temperature in the FP of cyclooctadiene (COD) through the conversion of some of the reaction heat into energy absorbed by the phase-transforming microparticles; and (2) to show how the amplitude and wavelength of FP-driven thermal instabilities can be tuned by the presence of phase-transforming microparticles, thereby providing a potential methodology to achieve patterning in thermoset polymers and composites.

Poly-(caprolactone) (PCL) with a combination of proper melting point ~60 °C, large melting enthalpy 139 J/g, and high compatibility with the COD is expected to interact with the polymerizing front effectively and hence selected as the demonstrative phase-transforming material in the present study. The effects of the environmental temperature and the volume fraction of microparticles on the front velocity and temperature are investigated through a one-dimensional (1D) parametric numerical study, whose results are confirmed by theoretical predictions and experimental observations. In particular, we show how heat absorption associated with phase-transforming microparticles reduces the amplitude, wavelength, and order of the pulsating instabilities and describe this effect in terms of a reduction of the Zeldovich number[35] used in previous studies to characterize the onset and order of FP-driven instabilities.

3.2 Numerical results of bulk and frontal polymerization.

3.2.1 Results and discussion

The competition between the energy absorbed by the melting of the particles and the energy generated by the exothermic reaction in the COD resin can first be analyzed within the context of bulk polymerization, i.e., in the absence of the thermal diffusion term in (4). Results from these so-called '0D simulations' based on the coupled ordinary differential equations (ODEs) for the temperature T, COD degree of cure α, and degree of PCL microparticle melt δ are presented in Figure 7 for the parameter values listed in Tables 3 and 4, and for initial values (T_0, α_0, δ_0) = (23 °C, 0.01, 0.01).

Figure 7a compares the evolution of the degree of melting δ with the degree of cure α for seven values of the particle volume fraction ϕ. In all cases, δ remains initially small as α increases,

leading to the early increase of the temperature T (Figure 7b). When T approaches the melting temperature of PCL (~60 °C), the phase transformation of the particles is initiated, reflected by a rapid increase of δ and a decrease in the slope of the $T - \alpha$ curves. After the melting is completed ($\delta = 1$), the exothermic reaction in the COD resumes. An increase in ϕ corresponds to a reduction in the available heat of reaction $\rho_r H_r(1 - \phi)$ and an increase in the absorbed heat $\rho_p H_p \phi$ due to the phase transformation of the particles. As ϕ increases, the initiation of melting thus takes place at higher values of α and the front temperature corresponding to the completion of the curing of COD resin ($\alpha = 1$) and the melting of PCL ($\delta = 1$) decreases. For this COD/PCL system, the critical value of ϕ for which the available heat of reaction equals the required heat absorption, i.e., for which $\rho_r H_r(1 - \phi_{crit}) = \rho_p H_p \ \phi_{crit}$ is found to be $\phi_{crit} = 0.55$. As apparent in Figure 7b, the system will become endothermic for $\phi > \phi_{crit}$.

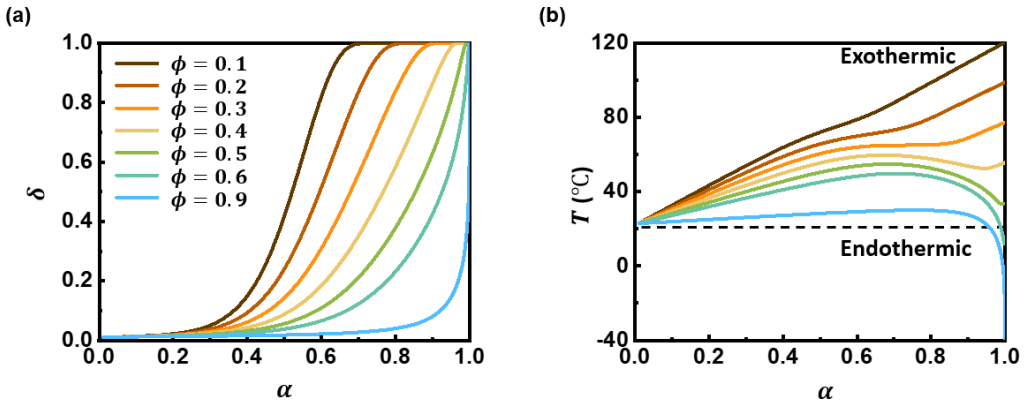

Figure 7. Diffusion-free 'bulk polymerization' of the COD/PCL system. Degree of cure α versus degree of melting δ (a) and versus temperature T (b) for different values of the microparticle volume fraction ϕ.

This simple '0D model' does not capture the sharp gradients present in the vicinity of the front and the contribution of the thermal diffusion process needed to drive the frontal polymerization. To model the impact of the PCL microparticles on the propagation of the

polymerization front, we solve the system of coupled PDEs described by equation (4) in a 1-D domain of length l = 40 mm, with the same thermal trigger in equation (2).

Figure 8a, c present snapshots of the profiles of temperature, degree of cure, and degree of melting obtained for ϕ = 0.05 and 0.15. For this homogenized model, the normalized temperature is defined as $\theta = \frac{T-T_0}{T_f-T_0}$ with T_f denoting the front temperature obtained by

$$T_f = T_0 + \frac{\rho_r H_r(1-\phi)-\rho_p H_p \phi}{\overline{\rho C_p}} \tag{6}$$

As before, the thermal front precedes the degree-of-cure front since the cure kinetics is thermally driven. The profile in δ is sharper than that in α indicating that the phase transition, although being driven by the heat of reaction, takes place faster than the polymerization as alluded to in Figure 7a. As apparent in Figure 8c, the thermal front becomes less sharp and the front velocity decreases as the particle volume fraction increases.

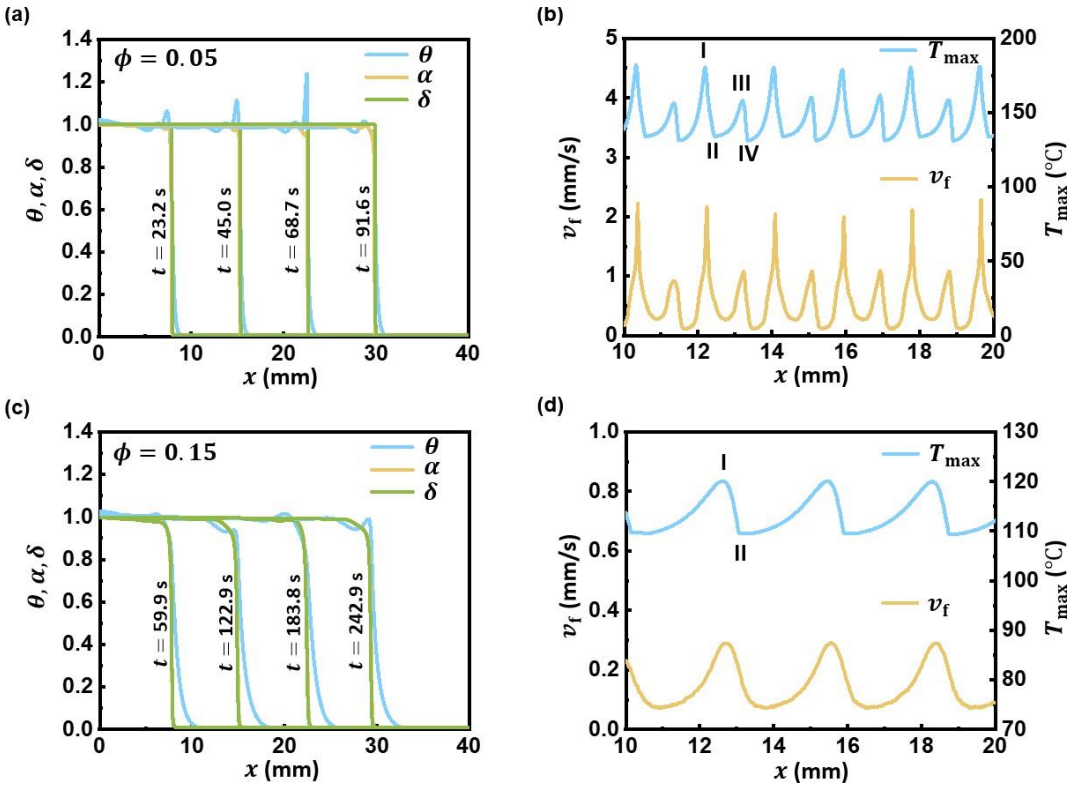

Figure 8. FP in COD with PCL microparticles predicted by the homogenized model. (a,c) Profiles of the normalized temperature θ, the degree of cure α, and the degree of melting δ for $\phi = 0.05$ and 0.15. (b,d) Spatial profiles of the instantaneous front velocity v_f and maximum temperature T_{max}.

The thermal spikes for which $\theta > 1$ confirm the existence of pulsating instabilities, as illustrated in Figure 8b, d, which present the spatial variation of the maximum temperature T_{max} and front velocity v_f along the path of the front. A direct correlation can be observed between the peaks and valleys in T_{max} and v_f. For the case $\phi = 0.05$, we obtain a period-4 oscillation marked as I, II, III, and IV in Figure 8b. The solution obtained for $\phi = 0.15$ is quite different, with the 'repeating unit' of v_f and T_{max} displaying a period-2 oscillation marked by I and II in Figure 8d. Moreover, as further discussed in the next section, the average front velocity and temperature are strongly affected by the particle volume fraction.

Effects of initial temperature and microparticle volume fraction

As shown earlier, the key features (front velocity, temperature, and instabilities) of FP in the COD/PCL system depend on the energy released by the chemical reaction and the amount of heat absorbed by the phase transition. We present hereafter the results of a parametric study on the effects of the microparticle volume fraction and the initial temperature of the resin on these key FP features. Figure 9a and 9b present the dependence of the average front velocity $\overline{v_f}$ and of the front temperature T_f on the particle volume fraction ϕ and the initial temperature T_0, with $\overline{v_f}$ computed based on the time needed for the front to travel between x = 10 mm and x = 30 mm. An increased amount of microparticles rapidly slows down the front and strongly reduces its temperature. And, as expected, higher values of the initial temperature lead to faster fronts.

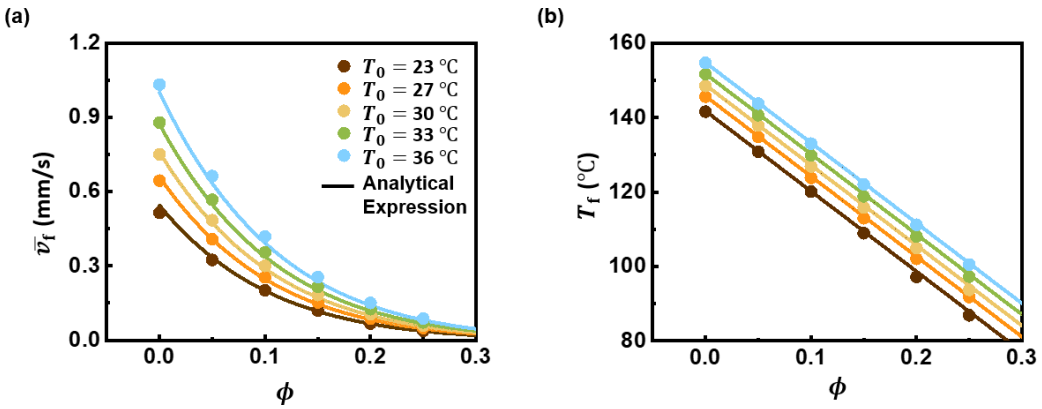

Figure 9. Effect of microparticle volume fraction ϕ and initial temperature T_0 on the average front velocity $\overline{v_f}$ (a) and the front temperature T_f (b). Circles: numerical predictions; Curves: analytical expressions with equation (6).

The numerical results shown as symbols in Figure 9a can be captured through the following analytical approximation $\overline{v_f}$ for the front velocity:[41-43]

$$V_f = \max_{\varepsilon} \sqrt{\frac{A_r \overline{\kappa}}{\rho_r H_r (1-\phi) - \rho_p H_p \phi} \frac{R\hat{T}(\varepsilon)^2}{E_r} \exp\left(\frac{-E_r}{R\hat{T}(\varepsilon)}\right) \frac{1}{\Pi[m, n, \alpha_0, \varepsilon]}} \quad (7)$$

where $\hat{T}(\epsilon) = T_0 + \frac{(1-\alpha_0-\epsilon)\left(\rho_r H_r(1-\phi)-\rho_p H_p \phi\right)}{\overline{\rho C_p}}$ is the effective front temperature of the instantaneous energy release, $\Pi[m, n, \alpha_0, \epsilon] = \int_0^{1-\epsilon-\alpha_0} \frac{y}{(y+\epsilon)^n (1-\epsilon-y)^m}\, dy$ is a coefficient with a form determined by the general Prout-Tompkins model, and ϵ between 0 and $1 - \alpha_0$ is the degree of cure at the instantaneous energy release.[43] The analytical values of the front velocity provided by (7) (solid curves) agree well with the numerical results (symbols) for all values of T_0. Similarly, Figure 9b shows a good agreement between the numerical values of T_f (symbols) and the analytical expression given by (6) (solid curves).

Turning our attention to the relationship between microparticle volume fraction and instabilities, we adopt the temperature ratio T_{max}/T_f (both expressed in K) to quantify the amplitude of the thermal instabilities. Figure 10 presents the dependence of the temperature ratio on ϕ and T_0, showing that the addition of phase-changing particles rapidly reduces and eventually eliminates (for $\phi \geq 0.2$) the FP-driven instabilities. In addition, the higher the initial temperature of the resin, the lower the amplitude of the thermal instabilities as was observed in DCPD[27] and methacrylic acid.[44] A detailed analysis of these results yields three modes of pulsating instabilities as illustrated in the insets of Figure 10b: period-2 instabilities (triangles), period-4 instabilities (squares), and higher-order instabilities (stars). The first inset (circle) shows the stable propagation for reference.

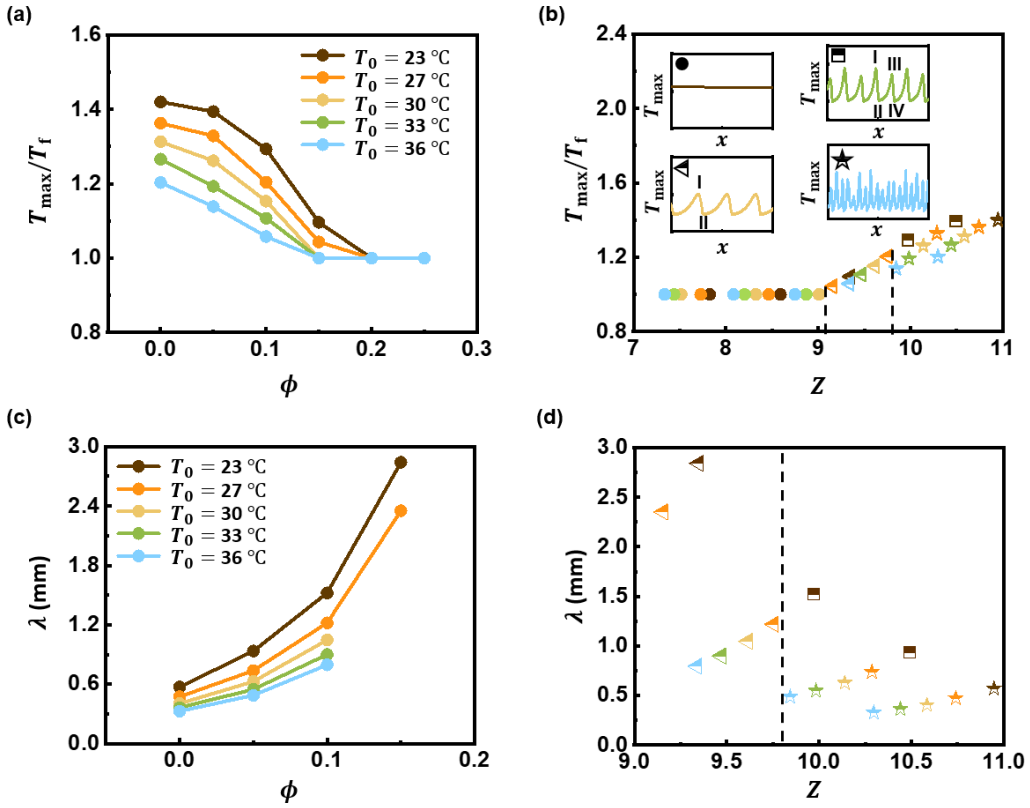

Figure 10. Effect of microparticle volume fraction ϕ and initial temperature T_0 on FP-driven instabilities. Temperature ratio T_{max}/T_f versus (a) ϕ and (b) the Zeldovich number Z for five values of the initial temperature T_0. The insets in (b) show characteristic T_{max} profile illustrating different modes of front propagation including stable propagation (circles), period-2 instability (triangles), period-4 instability (squares), and higher-order instability (stars). Dependence of the wavelength of instabilities λ on ϕ (c) and Z (d). The significance of the symbols in (d) is the same as in (b).

Figure 10b shows how the temperature ratio T_{max}/T_f relates to the Zeldovich number, which has long been used to characterize the onset of instability:[26, 44, 45]

$$Z = \frac{T_f - T_0}{T_f}\frac{E_r}{RT_f} \tag{8}$$

As apparent in that figure, the temperature ratio decreases with Z and the pulsating instabilities disappear for $Z < 9.1$. Moreover, for $9.1 < Z < 9.75$, period-2 pulsating instabilities are observed, while period-4 and higher-order instabilities are obtained for $Z > 9.75$. As microparticles suppress the

FP-driven instabilities at a higher ϕ, v_f is also significantly reduced on compromise. However, a larger v_f can be maintained at a higher initial temperature T_0 (Figure B1).

Figure 10c focuses on the dependence of the wavelength λ of these instabilities on ϕ and T_0. An increase in particle content leads to an increase in λ defined as the average distance between adjacent peaks in the maximum temperature profile. The discontinuous dependence of λ on Z presented in Figure 10d corresponds to the aforementioned transitions between instability modes.

3.2.2 Methods

Modeling of FP in the presence of phase-changing microparticles

FP in neat COD resin: FP in neat COD resin (denoted hereafter by the subscript r) in a 2-D domain can be described by the following reaction-diffusion partial differential equations (PDEs) written in terms of the temperature T (in K) and degree of cure α (non-dimensional) fields:

$$\begin{cases} \kappa_{\mathrm{r}}\dfrac{\partial^2 T}{\partial x^2}+\kappa_{\mathrm{r}}\dfrac{\partial^2 T}{\partial y^2}+\rho_{\mathrm{r}}H_{\mathrm{r}}\dfrac{\partial \alpha}{\partial t}=\rho_{\mathrm{r}}C_{p,\mathrm{r}}\dfrac{\partial T}{\partial t}, \\ \dfrac{\partial \alpha}{\partial t}=A_{\mathrm{r}}\exp(-\dfrac{E_{\mathrm{r}}}{RT})(1-\alpha)^n\alpha^m. \end{cases} \tag{1}$$

In (1), κ_r (in W/m · K), $C_{p,\mathrm{r}}$ (in J/kg · K), and ρ_{r} (in kg/m^3) respectively denote the thermal conductivity, heat capacity, and density of COD and are listed in the first row of Table 3,[34,36] while H_{r} (in J/kg) is the amount of heat generated by the exothermic reaction of the resin. The second relation approximates the cure kinetics of COD written with the generalized Prout-Tompkins model,[34] with A_{r} (in /s), E_{r} (in J/mol), and R (= 8.314 J/mol · K) respectively denoting the pre-exponential factor, activation energy, and ideal gas constant. n and m correspond to the reaction order. These parameters are summarized in the first row of Table 4.

Table 3: Thermal conductivity, density, and heat capacity of COD and PCL.[34,36]

	κ (W/m·K)	ρ (kg/m^3)	C_p (J/kg·K)
COD resin (r)	0.133	882.0	1838.5
PCL particles (p)	0.140	1145	1409.5

The C_p variation in PCL caused by the phase transition is not considered.

Table 4: Parameters approximating the cure kinetics of COD in (1) and the melting kinetics of PCL in (3).[34,37]

	A (1/s)	E (J/mol)	H (J/kg)	n	m
COD resin (r)	2.13×10^{19}	132, 000	220, 596	2.51	0.82
PCL particles (p)	4.94×10^{35}	241, 000	139, 000	–	–

To simulate the positive *x*-direction FP in the domain $0 \le x \le l$, $0 \le y \le w$, we adopt the following initial and boundary conditions:

$$\begin{cases} T(x,y,0) = T_0, & 0 \le x \le l, \quad 0 \le y \le w \\ \alpha(x,y,0) = \alpha_0, & 0 \le x \le l, \quad 0 \le y \le w \\ T(0,y,t) = T_{\text{trig}}, & 0 \le y \le w, \quad 0 \le t \le t_{\text{trig}}, \\ \dfrac{\partial T}{\partial x}(0,y,t) = 0 & 0 \le y \le w, \quad t > t_{\text{trig}}, \end{cases} \tag{2}$$

where T_0 (set at 23 ˚C), α_0 (= 0.01), T_{trig} (= 175 ˚C), and t_{trig} (= 5 s) respectively denote the initial temperature, the initial degree of cure, the triggering temperature, and the triggering time. Adiabatic boundary conditions are applied at all other boundaries. The Multiphysics Object-Oriented Simulation Environment (MOOSE),[38] an open-source C++ finite element solver that incorporates robust mesh and time step adaptivity modules needed to capture the sharp gradients in the vicinity of the moving front, is adopted in the simulations described hereafter.

Figure 11a presents thermal and degree-of-cure solutions along the front propagating *x*-direction at different times *t*, with the temperature *T* normalized as $\theta = \frac{T-T_0}{T_f-T_0}$, where $T_f = T_0 + \frac{H_r(1-\alpha_0)}{C_{p,r}}$ denotes the 'stable' temperature behind the front. The profiles of temperature and degree of cure show the presence of thermal instabilities leading to substantial thermal spikes ($\theta > 1$) as shown in the inset. Since the chemical reaction is driven by the Arrhenius term in the cure kinetics model described by (1), the thermal front is always slightly ahead of the degree-of-cure front.

As shown in Figure 11b, these thermal instabilities are also associated with a complex pulsating evolution of the width of the thermal front defined by $L_\theta = \max(\theta)/\max(d\theta/dx)$[17] around its average value $\overline{L_\theta}$ = 0.29 mm denoted by the solid horizontal line.

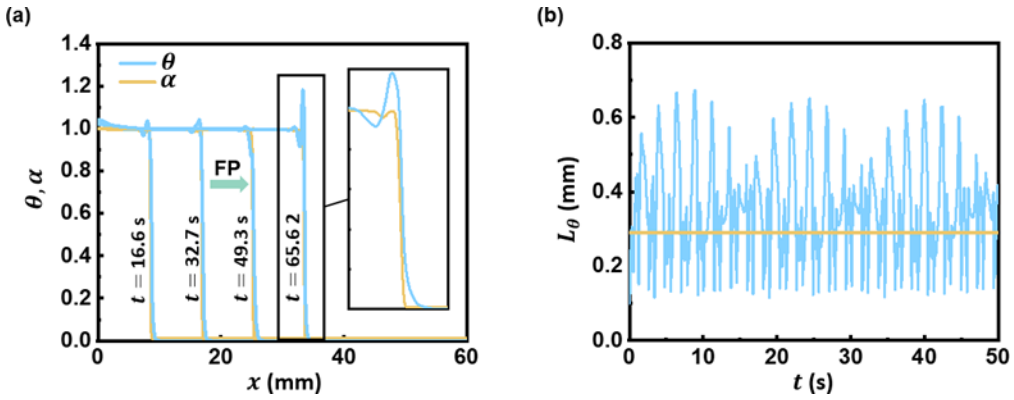

Figure 11. Frontal polymerization of COD. (a) Profiles of normalized temperature θ and degree of cure α at several moments during the right-traveling propagation of the polymerization front. (b) Pulsating evolution of the width L_θ of the thermal front, with the horizontal line denoting the average value $\overline{L_\theta}$.

Discrete and homogenized models of FP in COD mixed with PCL microparticles

We investigate the applicability of a homogenized model of FP in nano-particle-filled COD by performing first a set of simulations of FP in a domain composed of discrete PCL particles of increasingly smaller size embedded in a COD resin (Figure 12a).

The solution in the discrete phase-changing PCL particles (denoted hereafter with the subscript p) is obtained with the aid of the following melting-diffusion model describing the evolution of the degree of melting δ:

$$\begin{cases} \kappa_{\mathrm{p}}\dfrac{\partial^2 T}{\partial x^2}+\kappa_{\mathrm{p}}\dfrac{\partial^2 T}{\partial y^2}-\rho_{\mathrm{p}}H_{\mathrm{p}}\dfrac{\partial \delta}{\partial t}=\rho_{\mathrm{p}}C_{p,\mathrm{p}}\dfrac{\partial T}{\partial t}, \\ \dfrac{\partial \delta}{\partial t}=A_{\mathrm{p}}\exp(-\dfrac{E_{\mathrm{p}}}{RT})(1-\delta). \end{cases} \tag{3}$$

In the first equation, H_{p} denotes the melting enthalpy, and the negative sign reflects the endothermic nature of the melting process. The second equation approximates the phase transition of the PCL as a first-order kinetic model, where A_{p} and E_{p} respectively stand for the pre-

exponential constant and the activation energy of the melting process.[37,39] The thermal properties and melting kinetics parameters are listed in Table 3 and Table 4, respectively.

Equations (1) in the COD resin and (3) in the part of the domain occupied by the embedded PCL particles are solved in rectangular domain shown schematically in Figure 12a while maintaining the particle volume fraction ϕ fixed (ϕ = 0.1). The discrete model simulations involve a domain length l = 20 mm and three pairs of particle radius r and domain width w values (given in mm): (r, w) = (0.125, 1), (0.0625, 0.5), and (0.03125, 0.25). The evolution of the front location x_f defined as the location where α = 0.5 along the mid-line (dashed horizontal line (y = 0.5 w) in Figure 12a) is shown in Figure 12b, with the particle radius normalized by the average front width $\overline{L_\theta}$ introduced in Figure 11b. The initial degree of melting δ_0 is set as 0.01.

As apparent in Figure 12b, the predicted evolution of the front location becomes independent of the particle size when the particles become smaller than about 20% of the front width. This result suggests the introduction of a homogenized reaction-melting-diffusion model that simultaneously captures the energy created by the exothermic polymerization of the resin and the energy absorbed by the homogeneously mixed microparticles as

$$\begin{cases} \overline{\kappa}\dfrac{\partial^2 T}{\partial x^2} + (1-\phi)\rho_{\mathrm{r}} H_{\mathrm{r}} \dfrac{\partial \alpha}{\partial t} - \phi \rho_{\mathrm{p}} H_{\mathrm{p}} \dfrac{\partial \delta}{\partial t} = \overline{\rho C_p}\dfrac{\partial T}{\partial t}, \\ \dfrac{\partial \alpha}{\partial t} = A_{\mathrm{r}} \exp(-\dfrac{E_{\mathrm{r}}}{RT})(1-\alpha)^n \alpha^m, \\ \dfrac{\partial \delta}{\partial t} = A_{\mathrm{p}} \exp(-\dfrac{E_{\mathrm{p}}}{RT})(1-\delta). \end{cases} \tag{4}$$

The overbar quantities denote the homogenized material properties defined by

$$\begin{cases} \overline{\rho C_p} = \rho_r C_{p,r}(1-\phi) + \rho_p C_{p,p}\phi \text{ (Rule of mixture)}, \\ \overline{\kappa} = \kappa_r + \frac{3\kappa_r\phi}{(\frac{\kappa_p+2\kappa_r}{\kappa_p-\kappa_r})-\phi} \text{ (Maxwell model)}. \end{cases} \quad (5)$$

As shown in Figure 12b, the front propagation predicted by the homogenized model agrees well with that obtained with discrete model with PCL particles smaller than approximately 20% of the average thickness of the thermal front. This model is thus adopted for all simulation results presented in the remainder of this manuscript.

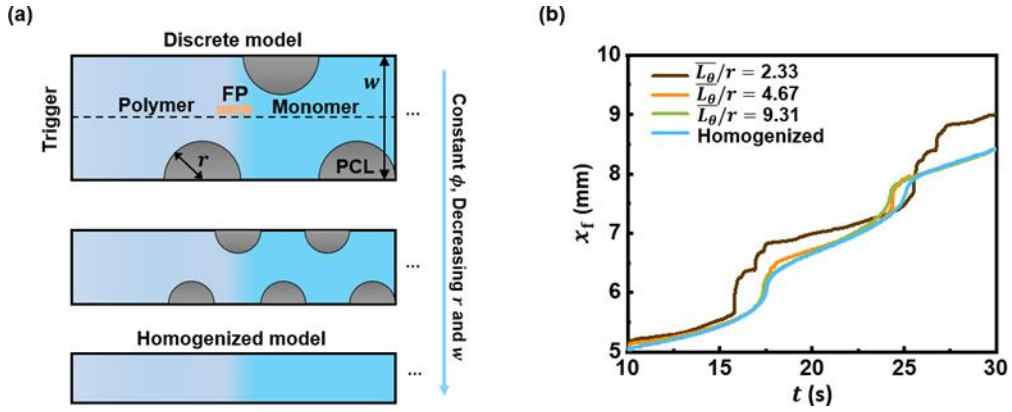

Figure 12. Discrete and homogenized models of FP in COD with PCL particles. (a) Schematics of discrete and homogenized models. (b) Comparison between the evolution of the front position x_f predicted by the discrete and homogeneous models.

3.3 Experimental validation

3.3.1 Results and discussion

To verify the numerical findings, experiments of FP with PCL microparticles were performed in test tubes, as exemplified by Figure 13a, where the volume fraction of microparticles ϕ = 0.1. At t = 0 s, a visible front is triggered by a soldering iron, propagating downward at an

averaged velocity of ~ 0.2 mm/s, transforming liquid COD monomers (in pink) to solid polybutadiene (in yellow). After FP, the samples are lacking visible defects. A Scanning Electron Microscope (SEM) photo of PCL microparticles is presented in Figure 13b, the scale bar represents 100 μm. The size distribution analysis indicates that the diameter of PCL micro particles ranges from 4.3 to 29.2 μm with an averaged particle diameter d of 15.5 ± 6.0 μm, which justifies the usage of the homogeneous model in (4) (Figure 12b). Differential scanning calorimetry (DSC) measurements are demonstrated in Figure B2, which verify the melting kinetics approximated by (3) but indicate a lower H_p of 89 ± 2.0 J/g compared to that of PCL with 100% crystallinity (Table 3).

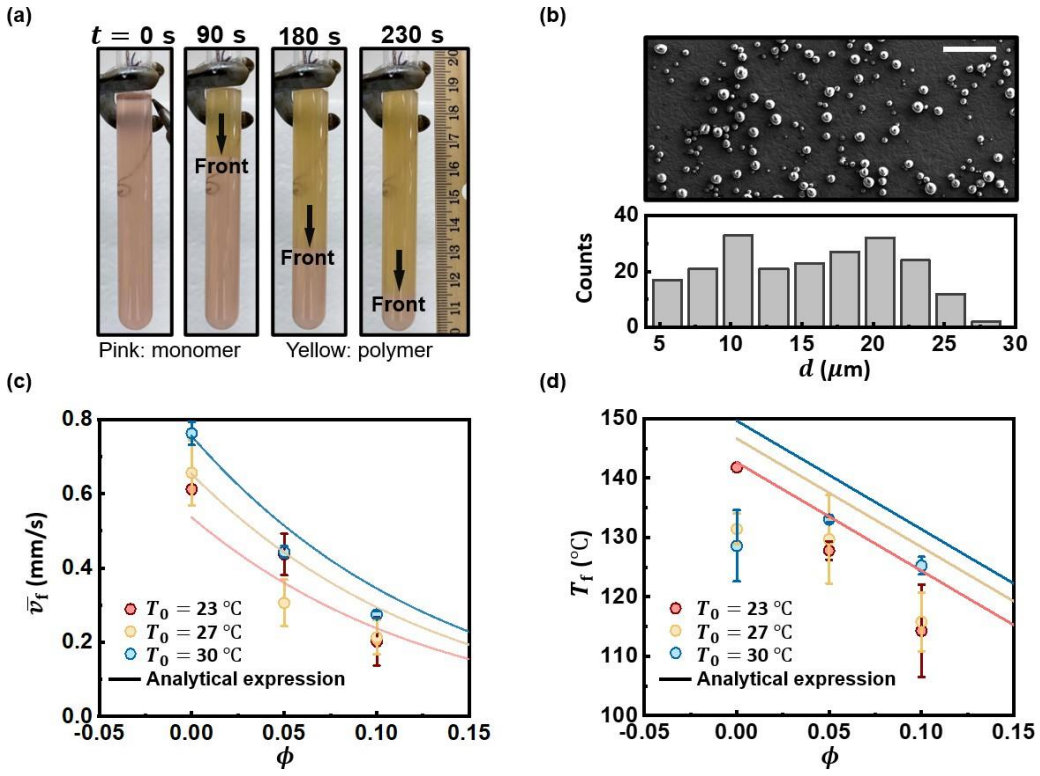

Figure 13. Experiments of FP with PCL microparticles. (a) Optical images of FP with PCL microparticles in a test tube with a volume fraction of microparticles ϕ = 0.1. The front is propagating downward (black arrows), transforming monomer (in pink) into polymer (in yellow). (b) SEM image of PCL microparticles with the scale bar representing 100 μm. A size distribution analysis indicates the averaged particle diameter d = 15.5 ± 6.0 μm. Average front velocity $\overline{v_f}$ and (d) front temperature T_f as functions of the microparticle volume fraction ϕ and the initial temperature T_0. The melting enthalpy H_p in analytical models is changed to 89 J/g.

The instabilities with mm-sized wavelength λ explored with numerical analyses are difficult to directly observe in experiments due to insufficient resolutions and the experimental results presented hereafter focus on the dependence of the front velocity on the particle volume fraction and initial temperature. Figure 13c shows that the average front velocity $\overline{v_f}$ measured in experiments (dots) increases with the initial temperature T_0 but decreases with the volume fraction ϕ of PCL microparticles, as suggested by the numerical results. Moreover, the experimental results of $\overline{v_f}$ are highly consistent with the analytical prediction given by (7) (solid lines). According to Figure 13d, the trends of front temperature measured by a thermocouple

with T_0 and ϕ generally agree with numerical and analytical findings. However, the experimental value is systematically lower than the analytical prediction given by (6) due to the heat loss to the surroundings,[46] which was not considered in the present modeling work.

3.3.2 Methods

Materials: 1,5 cyclooctadiene (COD) was purchased from Millipore-Sigma and was passed through a 1 cm plug of basic alumina to remove the octadecyl 3-(3,5-di-tert-butyl-4-hydroxyphenyl)propionate stabilizer. Polyvinyl alcohol (PVA, MW 13,000-23,000, 98% hydrolyzed), Tween-60, second- generation Grubbs catalyst (GC2), phenylcyclohexane, and tributyl phosphite (TBP) inhibitor were purchased from Sigma-Aldrich and used as received without further purification. Polycaprolactone (PCL, MW 50,000) powder was purchased from Polysciences.

Preparation of PCL microparticles: The methodology for the microparticle size reduction was adapted from Chen *et al*.[40] In a typical preparation, 1.0 g of PCL dissolved in 20 mL of methylene chloride composed the oil phase. This oil phase was added dropwise into 200 mL of 3% PVA solution (external aqueous phase) containing 0.05% of Tween-60 and stirred overnight at 700 rpm to form an O/W emulsion and then allow solvent evaporation. Finally, the produced microparticles were collected by centrifugation, washed with distilled water, and lyophilized by freeze-drying to obtain free-flowing powder-like PCL microparticles.

Morphology observation: The microparticles were dispersed in distilled water and air-dried onto a smooth silicon wafer chip substrate and observed using a Carl Zeiss Merlin scanning electron microscope. Particle size distribution was found by computer analysis using FIJI (ImageJ)

to be 15.5 ± 6.0 μm (count 212), below the threshold calculated for applicability to the homogeneous model described in the previous section.

Frontal polymerization: In a typical experiment, 3.125 mg GC2 is weighed out into an Eppendorf tube and dissolved in 156.25 μL phenylcyclohexane. One molar equivalent of TBP inhibitor with respect to GC2 is added to the solution via a volumetric syringe. Immediately prior to the combination, the PCL microparticles are dispersed in the COD via thorough vortexing and sonication. The catalyst/inhibitor solution is then added to 5 mL of COD (10,000 molar equivalents with respect to GC2) and mixed by inversions. 8 mL of the COD-PCL mixture is added to a test tube. A K-type thermocouple (Amprobe TMD-56) is submerged in the mixture to collect data and monitor temperature, which is controlled prior to initiation by submerging the test tube in gently cooled or heated water. Once the target initial temperature is reached, a soldering iron is used to initiate the frontal ring-opening metathesis polymerization (FROMP) reaction at the top of the volume, and the front propagates toward the bottom of the tube.

3.4 Conclusions

In this chapter with the aid of numerical analyses and experiments, we have shown how mixing PCL microparticles with COD resin affects the frontal polymerization process. A homogenized model of the resin/phase-changing particles system has been proposed and shown to be applicable for particle sizes inferior to about 20% of the average thermal front thickness. A parametric study has been carried out to investigate systematically the effects of the microparticles concentration and resin initial temperature on the frontal polymerization of COD, and in particular on the front velocity, temperature, and instability. Good agreement was found between numerical results, theoretical predictions, and experimental observations. These results

have illustrated how FP-driven instabilities can be harnessed by mixing endothermic phase-transforming microparticles, thereby providing a potential path for the efficient manufacturing of polymer and polymeric-matrix composites with controlled patterns and spatially dependent material properties.

3.5 References

(1) Robertson, I.; Yourdkhani, M.; Centellas, P.; Aw, J.; Ivanoff, D.; Goli, E.; Lloyd, E.; Dean, L.; Sottos, N.; Geubelle, P. et al. Rapid Energy-Efficient Manufacturing of Polymers and Composites via Frontal Polymerization. *Nature* **2018**, *557*, 223.

(2) Pojman, J.; Ilyashenko, V.; Khan, A. Free-Radical Frontal Polymerization: Self-Propagating Thermal Reaction Waves. *J. Chem. Soc., Faraday Trans.* **1996**, *92*, 2825– 2837.

(3) Mariani, A.; Bidali, S.; Fiori, S.; Sangermano, M.; Malucelli, G.; Bongiovanni, R.; Priola, A. UV-Ignited Frontal Polymerization of an Epoxy Resin. *J. Polym. Sci., Part A: Polym. Chem.* **2004**, *42*, 2066–2072.

(4) Frulloni, E.; Salinas, M.; Torre, L.; Mariani, A.; Kenny, J. Numerical Modeling and Experimental Study of the Frontal Polymerization of the Diglycidyl Ether of Bisphenol A/Diethylenetriamine Epoxy System. *J. Appl. Polym. Sci.* **2005**, *96*, 1756–1766.

(5) Mariani, A.; Fiori, S.; Chekanov, Y.; Pojman, J. Frontal Ring-Opening Metathesis Polymerization of Dicyclopentadiene. *Macromolecules* **2001**, *34*, 6539–6541.

(6) Liu, H.; Wei, H.; Moore, J. Frontal Ring-Opening Metathesis Copolymerization: Deviation of Front Velocity from Mixing Rules. *ACS Macro Lett.* **2019**, *8*, 846–851.

(7) Goli, E.; Robertson, I.; Geubelle, P.; Moore, J. Frontal Polymerization of Dicyclopentadiene: A Numerical Study. *J. Phys. Chem. B* **2018**, *122*, 4583–4591.

(8) Robertson, I.; Pruitt, E.; Moore, J. Frontal Ring-Opening Metathesis Polymerization of Exo-Dicyclopentadiene for Low Catalyst Loadings. *ACS Macro Lett.* **2016**, *5*, 593–596.

(9) Alzari, V.; Nuvoli, D.; Scognamillo, S.; Piccinini, M.; Gioffredi, E.; Malucelli, G.; Marceddu, S.; Sechi, M.; Sanna, V.; Mariani, A. Graphene-Containing Thermoresponsive Nanocomposite Hydrogels of Poly (N-isopropylacrylamide) Prepared by Frontal Polymerization. *J. Mater. Chem.* **2011**, *21*, 8727–8733.

(10) Mariani, A.; Fiori, S.; Bidali, S.; Alzari, V.; Malucelli, G. Frontal Polymerization of Diurethane Diacrylates. *J. Polym. Sci., Part A: Polym. Chem.* **2008**, *46*, 3344–3352.

(11) Fiori, S.; Mariani, A.; Ricco, L.; Russo, S. First Synthesis of a Polyurethane by Frontal Polymerization. *Macromolecules* **2003**, *36*, 2674–2679.

(12) Goli, E.; Parikh, N.; Yourdkhani, M.; Hibbard, N.; Moore, J.; Sottos, N.; Geubelle, P. Frontal Polymerization of Unidirectional Carbon-Fiber-Reinforced Composites. *Composites, Part A* **2020**, *130*, 105689.

(13) Dzhardimalieva, G. I.; Pomogailo, A. D.; Volpert, V. A. Frontal Polymerization of Metal-Containing Monomers: A Topical Review. *J. Inorg. Organomet. Polym.* **2002**, *12*, 1–21.

(14) Mota-Morales, J. D.; Gutiérrez, M. C.; Ferrer, M. L.; Jiménez, R.; Santiago, P.; Sanchez, I. C.; Terrones, M.; Del Monte, F.; Luna-Bárcenas, G. Synthesis of Macroporous Poly(acrylic

acid)–Carbon Nanotube Composites by Frontal Polymerization in Deep-Eutectic Solvents. *J. Mater. Chem. A* **2013**, *1*, 3970–3976.

(15) Gary, D. P.; Bynum, S.; Thompson, B. D.; Groce, B. R.; Sagona, A.; Hoffman, I. M.; Morejon-Garcia, C.; Weber, C.; Pojman, J. A. Thermal Transport and Chemical Effects of Fillers on Free-Radical Frontal Polymerization. *J. Polym. Sci.* **2020**, *58*, 2267–2277.

(16) Chechilo, N.; Enikolopyan, N. Effect of Pressure and Initial Temperature of the Reaction Mixture During Propagation of a Polymerization Reaction. *Dokl. Phys. Chem.* **1976**, *230*, 840–843.

(17) Vyas, S.; Goli, E.; Zhang, X.; Geubelle, P. Manufacturing of Unidirectional Glass-Fiber-Reinforced Composites via Frontal Polymerization: A Numerical Study. *Compos. Sci. Technol.* **2019**, *184*, 107832.

(18) Vyas, S.; Zhang, X.; Goli, E.; Geubelle, P. Frontal vs. Bulk Polymerization of Fiber-Reinforced Polymer-Matrix Composites. *Compos. Sci. Technol.* **2020**, 108303.

(19) Nason, C.; Roper, T.; Hoyle, C.; Pojman, J. UV-Induced Frontal Polymerization of Multifunctional (Meth)Acrylates. *Macromolecules* **2005**, *38*, 5506–5512.

(20) Chechilo, N.; Enikolopyan, N. Structure of the Front of the Polymerization Wave and the Mechanics of Propagation of Polymerization Reaction. Dokl. Akad. Nauk SSSR. 1974; pp 1131–1133.

(21) Robertson, I.; Pruitt, E.; Moore, J. Frontal Ring-Opening Metathesis Polymerization of Exo-Dicyclopentadiene for Low Catalyst Loadings. *ACS Macro Lett.* **2016**, *5*, 593–596.

(22) Chekanov, Y.; Pojman, J. Preparation of Functionally Gradient Materials via Frontal Polymerization. *J. Appl. Poly. Sci.* **2000**, *78*, 2398–2404.

(23) Nuvoli, D.; Alzari, V.; Pojman, J. A.; Sanna, V.; Ruiu, A.; Sanna, D.; Malucelli, G.; Mariani, A. Synthesis and Characterization of Functionally Gradient Materials Obtained by Frontal Polymerization. *ACS Appl. Mater. Interfaces* **2015**, *7*, 3600–3606.

(24) Chen, S.; Tian, Y.; Chen, L.; Hu, T. Epoxy Resin/Polyurethane Hybrid Networks Synthesized by Frontal Polymerization. *Chem. Mater.* **2006**, *18*, 2159–2163.

(25) Pojman, J.; Craven, R.; Khan, A.; West, W. Convective Instabilities in Traveling Fronts of Addition Polymerization. *J. Phys. Chem.* **1992**, *96*, 7466–7472.

(26) Bowden, G.; Garbey, M.; Ilyashenko, V.; Pojman, J.; Solovyov, S.; Taik, A.; Volpert, V. Effect of Convection on a Propagating Front with a Solid Product: Comparison of Theory and Experiments. *J. Phys. Chem. B* **1997**, *101*, 678–686.

(27) Goli, E.; Peterson, S. R.; Geubelle, P. Instabilities Driven by Frontal Polymerization in Thermosetting Polymers and Composites. *Composites, Part B* **2020**, *199*, 108306.

(28) Masere, J.; Stewart, F.; Meehan, T.; Pojman, J. Period-Doubling Behavior in Frontal Polymerization of Multifunctional Acrylates. *Chaos* **1999**, *9*, 315–322.

(29) Cardarelli, S.; Golovaty, D.; Gross, L.; Gyrya, V.; Zhu, J. A Numerical Study of One-Step Models of Polymerization: Frontal versus Bulk Mode. *Phys. D (Amsterdam, Neth.)* **2005**, *206*, 145–165.

(30) Comissiong, D.; Gross, L.; Volpert, V. Nonlinear Dynamics of Frontal Polymerization with Autoacceleration. *J. Eng. Math.* **2005**, *53*, 59–78.

(31) Inamdar, S.; Pujari, N.; Karimi, I.; Ponrathnam, S.; Tayal, R.; Kulkarni, B. Spinning Wave Motion in Frontal Polymerization. *Chem. Eng. Sci.* **2007**, *62*, 1448–1455.

(32) Pojman, J. A.; Masere, J.; Petretto, E.; Rustici, M.; Huh, D.-S.; Kim, M. S.; Volpert, V. The Effect of Reactor Geometry on Frontal polymerization spin modes. *Chaos* **2002**, *12*, 56–65.

(33) Riolfo, L.; Carballido-Landeira, J.; Bounds, C.; Pojman, J.; Kalliadasis, S.; De Wit, A. Experimental Reaction-Driven Liquid Film Fingering Instability. *Chem. Phys. Lett.* **2012**, *534*, 13–18.

(34) Lloyd, E.; Feinberg, E.; Gao, Y.; Peterson, S.; Soman, B.; Hemmer, J.; Dean, L.; Wu, Q.; Geubelle, P.; Sottos, N. et al. Spontaneous Patterning during Frontal Polymerization. *ACS Cent. Sci.* **2021**,

(35) Ilyashenko, B.; Pojman, J. Single-Head Spin Modes in Frontal Polymerization. *Chaos* **1998**, *8*, 285–289.

(36) Poly(caprolactone). https://polymerdatabase.com/polymers/polycaprolactone. html.

(37) Fraga-López, F.; Manuel Martínez-Ageitos, J.; Rodríguez-Núñez, E.; Blanco- Mendez, J.; Luzardo-Álvarez, A.; Calvo-Carnota, E.; Jiménez-Carrillo, L. The Mechanism and Energy of Activation of the Melting of Poly (ε-caprolactone) with and without Prior Treatment with Span 80. *J. Appl. Polym. Sci.* **2011**, *121*, 3635–3640.

(38) Gaston, D.; Newman, C.; Hansen, G.; Lebrun-Grandie, D. MOOSE: A Parallel Computational Framework for Coupled Systems of Nonlinear Equations. *Nucl. Eng. Des.* **2009**, *239*, 1768–1778.

(39) Gao, Y.; Dearborn, M.; Hemmer, J.; Wang, Z.; Esser-Kahn, A.; Geubelle, P. Controllable Frontal Polymerization and Spontaneous Patterning Enabled by Phase-Changing Particles. *Small.* **2021**, 17, 2102217.

(40) Chen, D.; Bei, J.; Wang, S. Polycaprolactone Microparticles and Their Biodegradation. *Polym. Degrad. Stab.* **2000**, *67*, 455–459.

(41) Novozhilov, B. Propagation Rate of the Front of an Exothermic Reaction in Condensed Phase. Doklady Akademii Nauk. 1961; pp 151–153.

(42) Garbey, M.; Taik, A.; Volpert, V. Linear Stability Analysis of Reaction Fronts in Liquids. *Quart. Appl. Math.* **1996**, *54*, 225–247.

(43) Kumar, A.; Gao, Y.; Geubelle, P. H. Analytical estimates of front velocity in the frontal polymerization of thermoset polymers and composites. *J. Polym. Sci.* **2021**, *59*, 1109– 1118.

(44) Solovyov, S.; Ilyashenko, V.; Pojman, J. Numerical Modeling of Self-Propagating Polymerization Fronts: The Role of Kinetics on Front Stability. *Chaos* **1997**, *7*, 331–340.

(45) Volpert, V.; Volpert, V.; Pojman, J.; Solovyov, S. Hydrodynamic Stability of A Polymerization Front. *Eur. J. Appl. Math.* **1996**, *7*, 303–320.

(46) Goli, E.; Gai, T.; Geubelle, P. Impact of Boundary Heat Losses on Frontal Polymerization. *J. Phys. Chem. B* **2020**, *124*, 6404–6411.

Chapter 4. Many-Point Laser Initiation for Manufacturing and Thermal Correction in Manufacturing

The previous Chapters have presented local and bulk tools for controlling the frontal profile, developed in conjunction with computational modeling systems to predictably generate patterns. Beyond manipulating the behavior of one or two fronts, the patterning design space can be greatly expanded by initiating many fronts to propagate toward many domains characterized by curing during thermal overlap. Complementary to using phase-change materials as a model heat sink, laser irradiation is used here as a heat source. Full control of position, irradiation area, irradiation time, and power delivered by a high-powered laser enable hands-free initiation or the addition of energy below the amount required for initiation for pre-heating or thermal correction in manufacturing. In this Chapter, we report the first instantaneous non-contact thermal initiation of FP and preliminary results toward many-point initiation, as well as a vision for the future of the ongoing work.

4.1 Introduction

The work toward realizing the morphogenic manufacturing potential of FP has centered around controlling heat transfer in the energy competition at the front. Functioning as the inhibitor morphogen in the RD system, the impact of heat loss inhibitor on the front was presented, both in the bulk via mixed endothermic microparticles or around discrete obstacles. Actions taken also led to activator morphogens, hot spots, present at frontal overlap, behind discrete obstacles, and within instabilities; however, a direct method of adding energy at target locations and times is missing from frontal polymerization. Throughout the history of the field, energy addition to fronts has been via bulk preheating to raise T_0 prior to initiation or thermal triggering at one or two points via physical contact with a heat source such as a soldering iron or resistive wire. This falls short of the goal of truly autonomous manufacturing as it requires manual input, limiting advanced patterning potential as the number of coupled reaction-diffusion waves is limited to the number of physical contacts.

In 2020, Dean *et al*, again within our collaboration, demonstrated the photoinitiation of FP of DCPD using photothermal heating of carbon nanoparticles; however, this initiation required "approximately two minutes" of irradiation prior to initiation. The Esser-Kahn group previously reported on using carbon black nanoparticles for localized photothermal heating.[1] Aside from time added to the manufacturing process, this has two critical shortcomings. First, the intentionally vague reported initiation time reveals significant variation between tests, likely due to inhomogeneities in photothermal nanoparticle mixing, heat transfer to the bulk in the liquid mixture, and the unfocused light source (from a large lamp).[2] Initiation time must be precise for controlling front travel distance. Front velocities of DCPD in this setting are ~ 1 mm/s; therefore, every 1 s difference in initiation time corresponds with a mm difference in predicted pattern

location. Having replicated the experiment with Dr. Zhao Wang, variation is significant such that the front initiated first propagates through the second irradiated area before second initiation can occur.[3] Temporal control of front position thus rapidly degrades with small variation in long initiation times due to the relatively fast front speed. Second, the long irradiation time prior to triggering allows time for heat to diffuse away from the initiation point, leading to excess energy in the system that cannot be accounted for with the level of precision required for controlled patterning, especially for patterns at small length scales. Given the observed variation, initiation must approach instantaneity at all points. Outside of thermal initiation, Stawiasz *et al* of our collaboration demonstrated noncontact photo-initiation of the FP of DCPD following 6 min low-power irradiation with 375 nm light. They hypothesized that the catalyst was activated by photoinduced phosphine or phosphite release from the inhibitor, subsequently triggering FP.[3] This approach prevents undesirable preheating, but still has unacceptable delay and variation to be viable for controlled RD patterning, where front shape and location in time determine the interactions between the front and additives or other fronts. Therefore, an instantaneous initiation mechanism needed to be developed for simultaneous noncontact multi-point initiation.

To satisfy the presented requirement of initiation approaching instantaneity, a high-powered laser was employed for rapid non-contact initiation of FP of DCPD, assisted by mixed photothermal heating of carbon nanoparticles. Andrés Cook of the Esser-Kahn and Squires groups built and operates the laser setup. We completed the work presented in this Chapter together, and he continues it. To date, we have demonstrated near-simultaneous initiation for three points in multiple configurations, and work is ongoing to synchronize initiations demonstrated for 4+ point systems. Beyond the capacity for precise initiation of many fronts, full spatiotemporal control of irradiation via programming of irradiation position, timing, and power enables the laser to operate

as an optimal heat source during FP as well. Ongoing work aims to demonstrate 1) initiation of delayed secondary fronts that may then travel shorter distances; 2) non-point heating along lines and shapes and of the bulk, before and during FP; and 3) localized heating during propagation for strategic acceleration and temperature elevation of a front, or prevention of quenching or thermal correction in manufacturing of parts with complex geometries subject to increased heat loss. We aim to develop a complete method for adding energy anywhere at any time for precise, programmable thermal patterning with FP.

4.2 Results and discussion

4.2.1 Many-point laser initiation: preliminary results

To demonstrate the potential for rapid initiation of FP with the high-powered laser setup, the laser was programmed to irradiate an increasing number of initiation points on a sample of DCPD mixed with 5 wt% carbon black (CB) nanoparticles in a radial geometry. Concerns with uneven mixing of CB nanoparticles[2] motivated using at least 5% CB as the optimal level for complete absorption. Initiation time suffered at higher loading levels due to the thermally conductive carbon black nanoparticles causing heat transfer away from the irradiation zone to dominate local absorption for activation of the reaction. Grubbs' catalyst concentration was doubled to expedite initiation, although this would decrease pot life from the 30 h achieved with the standard neat mixture. The laser position on the sample is controlled by a galvanometer (galvos), a series of two mirrors that reflect the beam, programmed for sub-microsecond changes of angle that translate to essentially instantaneous beam position control in x and y on the sample. In initial results, a 980 nm diode laser with 9 W max power was used with a 5 mm beam width.

Initial demonstrations with one and two initiation points are shown in Figure 14 and Movies S8 and S9. While it visibly appears as if the laser is on two points at once, it is oscillating between the two rapidly, essentially dwelling on each point for half the time. Therefore, the energy delivered to each of *n* points is equal to total energy divided by *n*. As expected, initiation times increase with more initiation points. The 1 s difference between the two points in Figure 14b leads to the visibly longer travel distance for the front initiated at point 1, which polymerized a larger area before colliding with the second front closer to point 2. The prevalence of variation is most apparent in the samples initiated at three points in Figure 15 and Movies S10 and S11. In Figure 15a, point 3, the bottom point of the triangle, initiates 4s before point 2 and 17s before point 1. The first front initiated polymerized most of the sample and then collided with the other two very near their initiation points. The three points in a line initiated much closer in time to each other, but in less than half the time required for those in the triangle configuration. Further work is ongoing to quantify the impact of separation distance between initiation points, although much of this difference is likely due to sample-to-sample variation. Overall, the initiation times achieved are the fastest and at the most points ever demonstrated without physical contact for FP; however, greater reduction is necessary for controlled programmable patterning. We expect current work to increase laser power and increase homogeneity of CB mixing will address these issues and push the number of achievable points much higher.

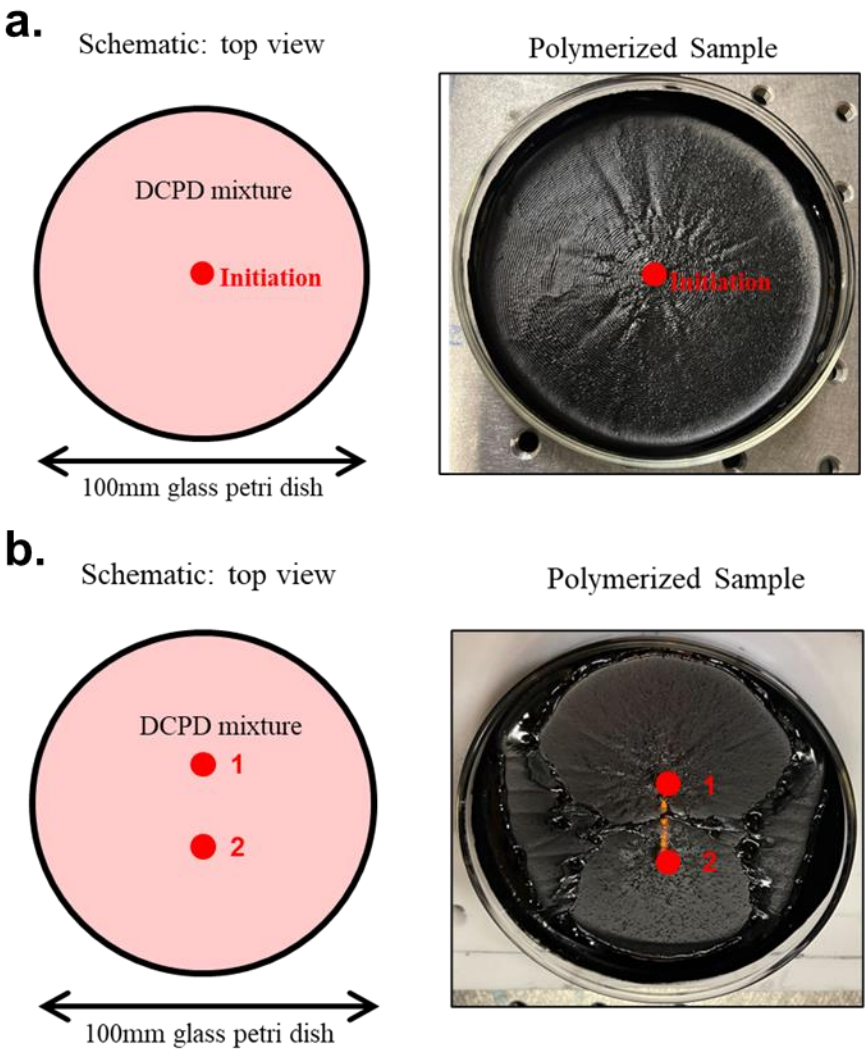

Figure 14. One- and two-point laser-initiated FP of 20 mL DCPD-5%CB, with initiation locations marked in red. a) Scheme for radial sample geometry with initiation in center, and photo of polymerized sample. Initiation time was < 5 s. b) Scheme showing location of two initiation points equidistant from the center and photo of polymerized sample. Initiation times were 1.5 s for point 1 and 2.5 s for point 2, leading to the visibly greater front travel distance from point 1.

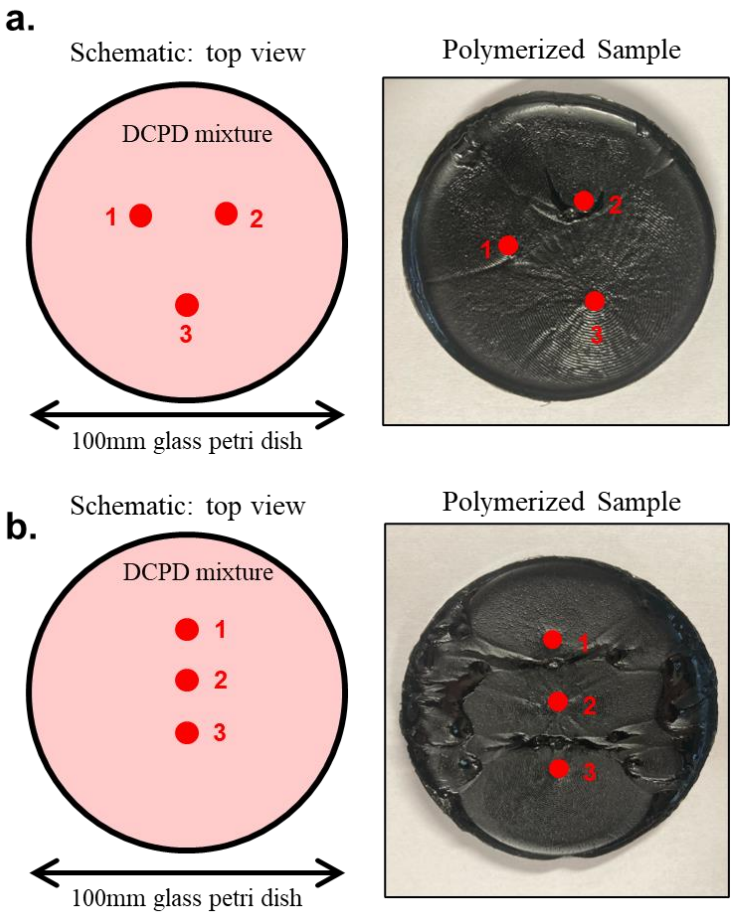

Figure 15. Three-point laser-initiated FP of 20 mL DCPD-5%CB, with initiation locations marked in red. a) Scheme for radial sample geometry with three initiation points in a triangle equidistant from the center, and photo of polymerized sample. Initiation times for points 1, 2, and 3 were 30, 21, and 17 s, respectively. b) Scheme showing location of three initiation points in a line and photo of polymerized sample. Initiation times for points 1, 2, and 3 were 12, 8.5, and 10 s, respectively.

4.2.2 Delayed initiation of additional fronts: ongoing work

While the noncontact initiation of many fronts represents a major expansion of the RD patterning design space for FP, addition of energy to the system need not be confined to prior to initiation. First, additional irradiation may initiate secondary fronts to be designed to propagate a shorter distance before frontal overlap, as envisioned in Figure 16, where a second initiation occurs 5 s after the first. Application of FP to widescale manufacturing is currently limited by areas of increased heat loss in real part geometries, such as when passing through the corner joint shown.

Rather than the front slowing as it passes through limited volume, secondary initiation is hypothesized to decrease overall fabrication time from 13 to 11 s in the conceptual schematic.

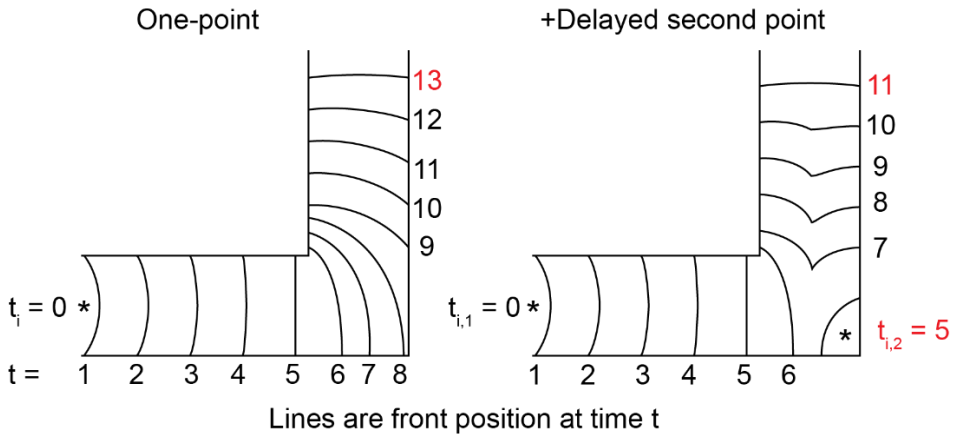

Figure 16. Conceptual front position in time progression as the front propagates through a corner joint with one front initiated at $t = 0$, compared with that plus a secondary initiation 5 s later. Lines represent the front position at the labeled t.

4.2.3 Non-point initiation and energy addition: ongoing work

Beyond initiation at multiple locations and times, energy may be supplied below the amount required to initiate a front. Using the laser's ability to change position rapidly, a region of the sample may be scanned or a shape traced, effectively heating the entirety of the area or along the trace. If uniformity of mechanical properties and thus avoidance of frontal overlap is desired, fabrication time may still be reduced by initiating along a line or shape. As shown in Figure 17, initiation along the proposed lines would leave a short distance for the front to travel, reducing the time significantly compared to initiation at a point on one end.

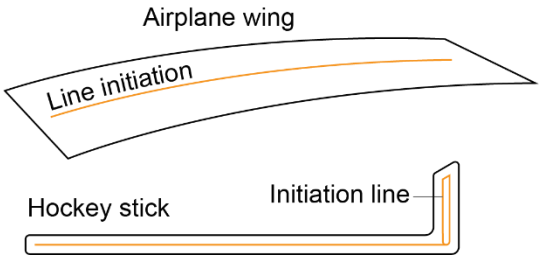

Figure 17. Conceptual schematic of non-point initiation along lines (orange) traced by the laser for rapid fabrication of two composite parts. The single, large front must only travel a short distance to the part boundaries, greatly reducing fabrication time without employing multiple fronts that would collide with elevated temperature.

Gentle irradiation of an area may be used for thermal correction of a front to address concerns of mechanical property variation due to variation in front energy throughout complex geometries. Strategic addition of energy can prevent quenching or slowing of the front, such as through the narrow joint conceptualized in Figure 18.

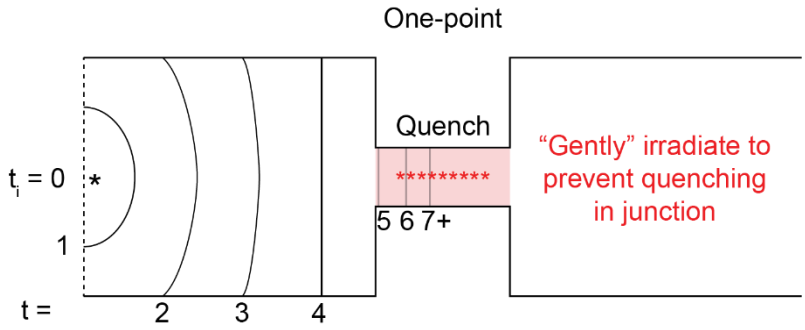

Figure 18. Front position in time conceptual progression as the front propagates through a narrow junction that would otherwise cause quenching of the front due to increased heat loss and less available unreacted exothermic monomer. Additional irradiation below the energy level required to initiate a front in the region shaded in red can be programmed to supply sufficient energy to prevent quenching. Lines represent the front position at the labeled *t*.

This can first be useful for manufacturing of parts with uniform mechanical properties, before expanding to more complex designs programmed for spatial variation in cure temperature. We envision eventual application to a dynamic read-write system, wherein computer vision monitors

the front for variance and can direct the appropriate amount of additional energy to correct the frontal profile to desired values. This automatic thermal corrective system is conceptualized in Figure 19.

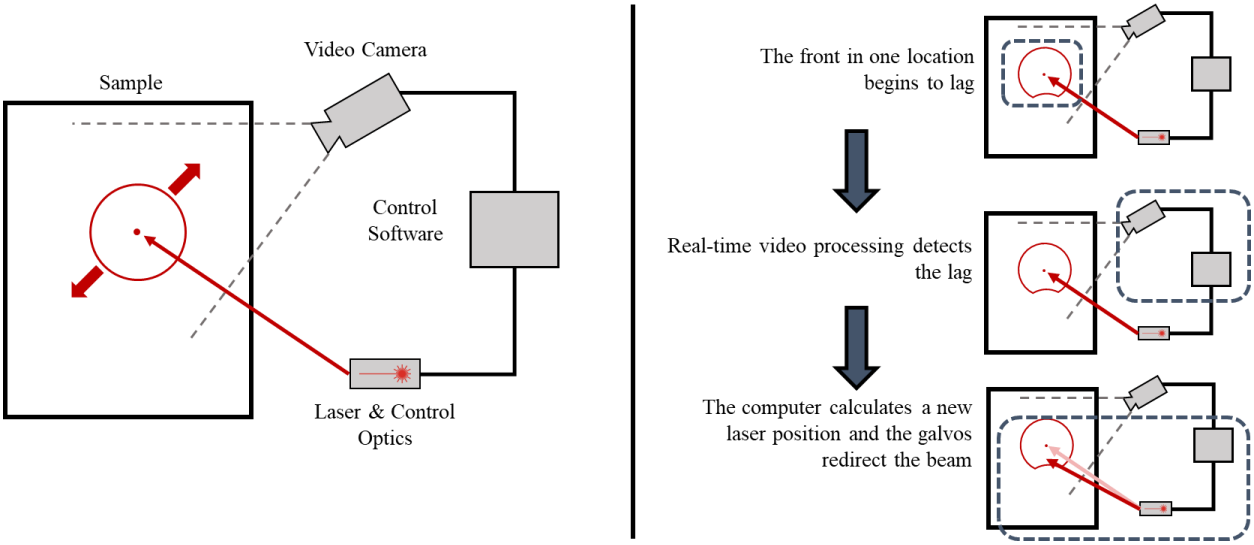

Figure 19. Conceptual schematic of an automatic thermal corrective system for detecting inconsistencies with expected front position and temperature and supplying the appropriate amount of energy for correction.

4.3 Methods

Laser set up: A 980 nm IR laser (MDL-N-980) with a maximum power of 8900 mW was purchased from Opto Engine LLC. The partially collimated beam is focused with a 250 mm focal length lens from Thorlabs. The laser follows a 2 m beam path before reflecting off QS15XY galvos from Thorlabs and traveling ~ 25 cm to the sample. The angle of the two galvos controls translation of the beam in two dimensions on the sample. The galvos are connected to a computer by a pair of MCP4725 digital-analog converters (DAC) from Adafruit, connected to an Arduino Nano. The laser has variable power output and was calibrated to 200 mW.

Materials: Dicyclopentadiene (DCPD), 5-ethylidene-2-norbornene (ENB), second-generation Grubbs' catalyst (GC2), phenylcyclohexane, and tributyl phosphite (TBP) inhibitor were purchased from Sigma-Aldrich and used as received without further purification. Vulcan XC72R conductive carbon black (CB) nanoparticles with an average primary particle size of 50 nm was generously provided by Cabot Corporation and used as received.

Resin preparation: Given that DCPD is solid at room temperature, it is first melted at 35 °C and mixed with 5 wt% ENB to depress the melting point and degassed at 28 kPa overnight. All references to DCPD herein refer to this 95/5 DCPD/ENB solution. 5 wt% CB is added to the DCPD, vortexed thoroughly, and sonicated for at least 30 min. GC2 (1:5000 molar equivalents with respect to DCPD) is dissolved in 400 μL phenylcyclohexane. One half molar equivalent of TBP inhibitor with respect to GC2 is added and the solution is vortexed and sonicated for 20 min. Immediately prior to addition to the reaction vessel and initiation of FP, the catalyst/inhibitor mixture is added to the DCPD/CB mixture and vortexed.

Frontal polymerization: FP experiments are conducted in a glass petri dish. The diameter of the dish is 100 mm and thickness of the sample is approximately 10 mm. A FLIR E8 Thermal Imaging Camera is adopted to monitor the temperature evolution. The laser is used to initiate the frontal ring-opening metathesis polymerization (FROMP) reaction.

4.4 Conclusions

In summary, we showed a novel approach to rapidly initiate multiple fronts without physical contact, including the first demonstration of instantaneous noncontact thermal initiation in FP. The ongoing approach to increasing the number of simultaneous initiation points was described, along with a conceptual vision for an automatic thermal corrective system. Thus far, we have relied on hotspots from frontal overlap and instabilities to create regions of elevated temperature curing. Spatiotemporal control of energy addition using a laser with variable power unlocks the potential for the "drawing" of regions or shapes of curing elevated to a target temperature or temperature distribution. The tool of energy addition to FP by laser is to be developed as the tools of energy withdrawal using model heat sinks were in Chapters 2 and 3, similarly expanding the design space for morphogenic manufacturing via FP. Computational modeling of these tools may then be combined with those developed in the previous Chapters to yield an expansive RD design space in FP capable of autonomously generating advanced patterns beyond modern manufacturing techniques.

4.5 References

(1) Steinhardt, R. C.; Steeves, T. M. C.; Wallace, B. M.; Moser, B.; Fishman, D. A.; Esser-Kahn, A. P. Photothermal Nanoparticle Initiation Enables Radical Polymerization and Yields Unique, Uniform Microfibers with Broad Spectrum Light. *ACS Applied Materials and Interfaces* **2017**. https://doi.org/10.1021/acsami.7b12230.

(2) Dean, L. M.; Ravindra, A.; Guo, A. X.; Yourdkhani, M.; Sottos, N. R. Photothermal Initiation of Frontal Polymerization Using Carbon Nanoparticles. *ACS Applied Polymer Materials* **2020**. https://doi.org/10.1021/acsapm.0c00726.

(3) Stawiasz, K.; et al. Photoexcitation of Grubbs' Second-Generation Catalyst Initiates Frontal Ring-Opening Metathesis Polymerization. *ACS Macro Lett.* **2020**, *9* (11), 1563–1568.

Appendix A: Supporting Information for Chapter 2: Controllable Frontal Polymerization and Spontaneous Patterning Enabled by Phase-Changing Particles

Regime design space in the plane of characteristic time length ratio and particle line fraction. According to Figure 2d in the main text, in the design space of regimes, a boundary separating Regime I, where FP is leading the melting-thermal diffusion effects (large t^*), versus Regime II, where melting-thermal diffusion effects are leading the FP (small t^*), is found at $t^* = 27$. At $t^* < 27$, another boundary $\phi = 0.6$ further discriminates Regimes II-a and II-b. Larger values of ϕ correspond to more heat absorption, less heat release, and lower temperature near the particle so that the front is reinitiated above the particle, leading to Regime II-b. Conversely, smaller values of ϕ lead to Regime II-a. However, when the particle size r is smaller than 1 mm, the high temperatures present behind the front lead to complete melting of the particle and reinitiate the front behind the particle. This scenario corresponds to Regime II-a even for the higher values of ϕ that are associated with Regime II-b for larger particles (Figure A2).

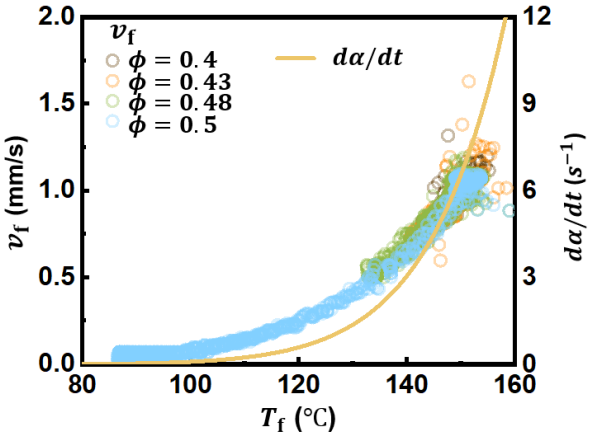

Figure A1. Correlation between the front temperature T_f, front velocity v_f, and reaction rate dα / dt. The data points result from FP simulations in several domains with different values of ϕ, indicated by different colors. The relationship between v_f and T_f is further supported by the temperature dependence of the reaction rate dα / dt obtained by plugging α = 0.5 and value of T_f into the cure kinetic model in equation (1).

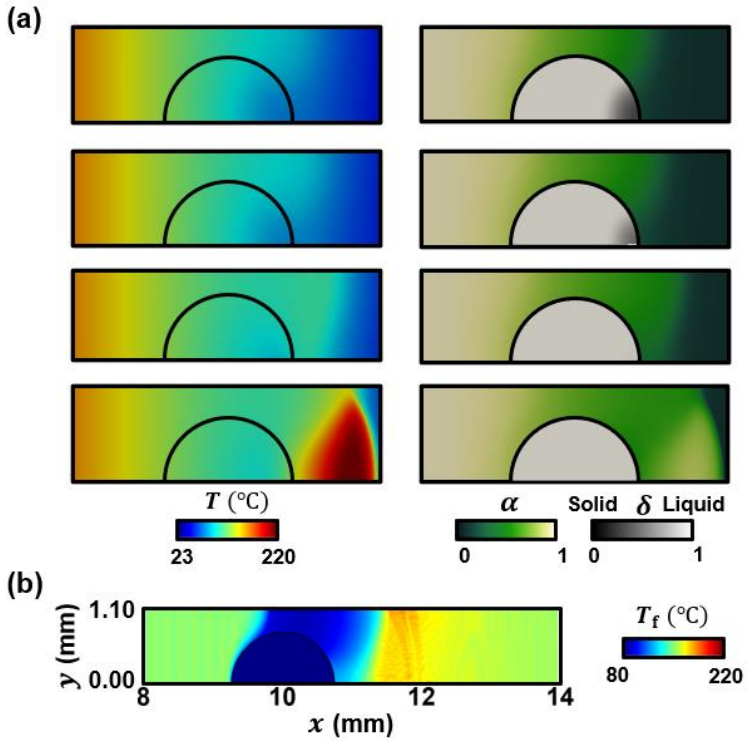

Figure A2. Regime II-a obtained with a small particle of radius r = 0.75 mm and a large value of the particle line fraction ϕ = 0.68. a) Contours of the temperature T, degree of cure α and degree of melting δ. Due to its small radius r, the particle rapidly heats up, pre-heats the resin, and reinitiates the front behind the particle. b) Contour of front temperature T_f characteristic of Regime II-a.

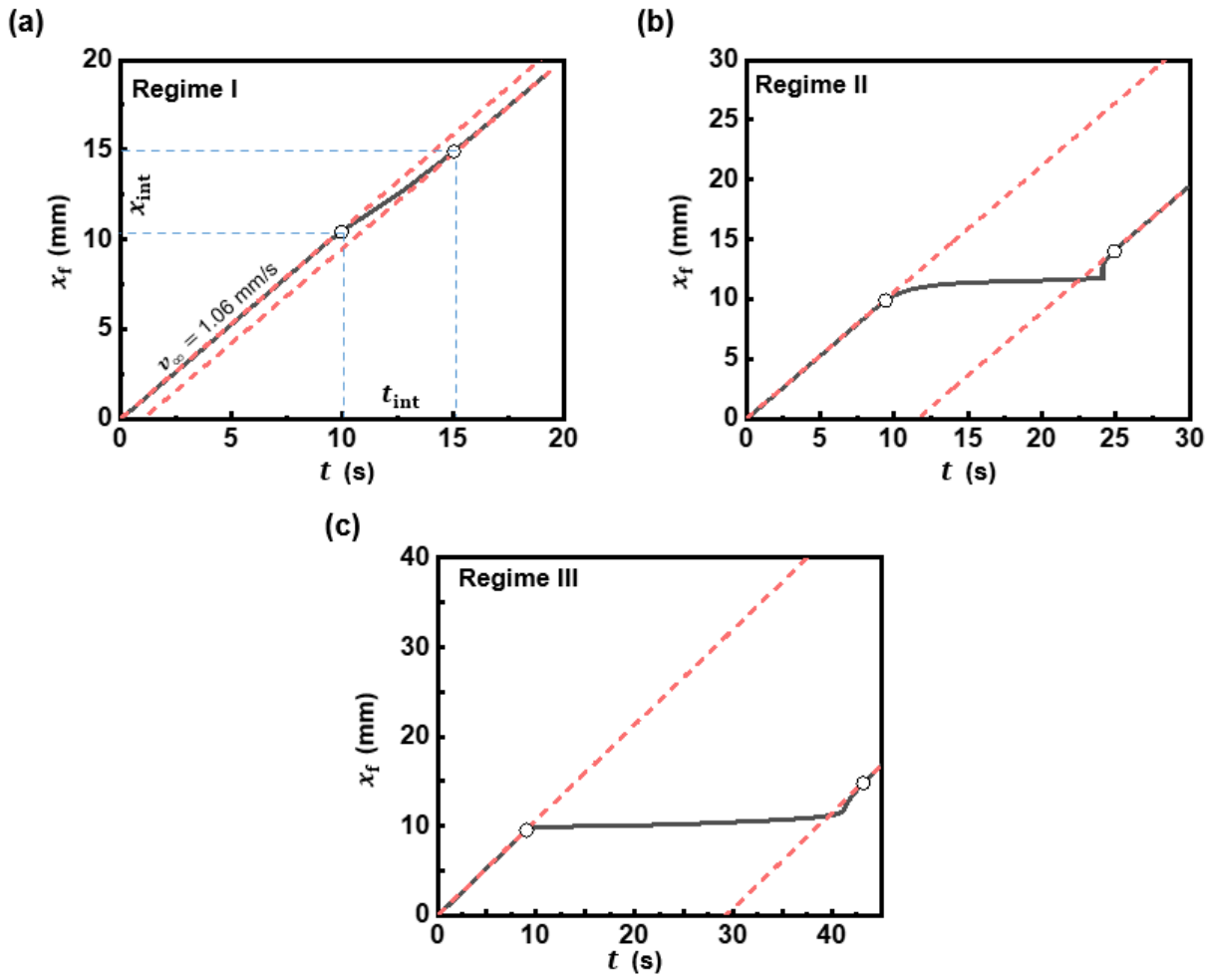

Figure A3. Definition of the front velocity v_{int} associated with the front-particle interaction. Evolution of the front location x_f in a) Regime I, b) Regime II-a, and c) Regime II-b. As illustrated in the Regime I figure, $v_{int} = x_{int} / t_{int}$ is the average velocity during the time interval t_{int} and distance x_{int} that define the deviation from the steady-state regimes (for which the front velocity $v_\infty = 1.06$ mm/s before and after the interaction of the front with the row of particles.

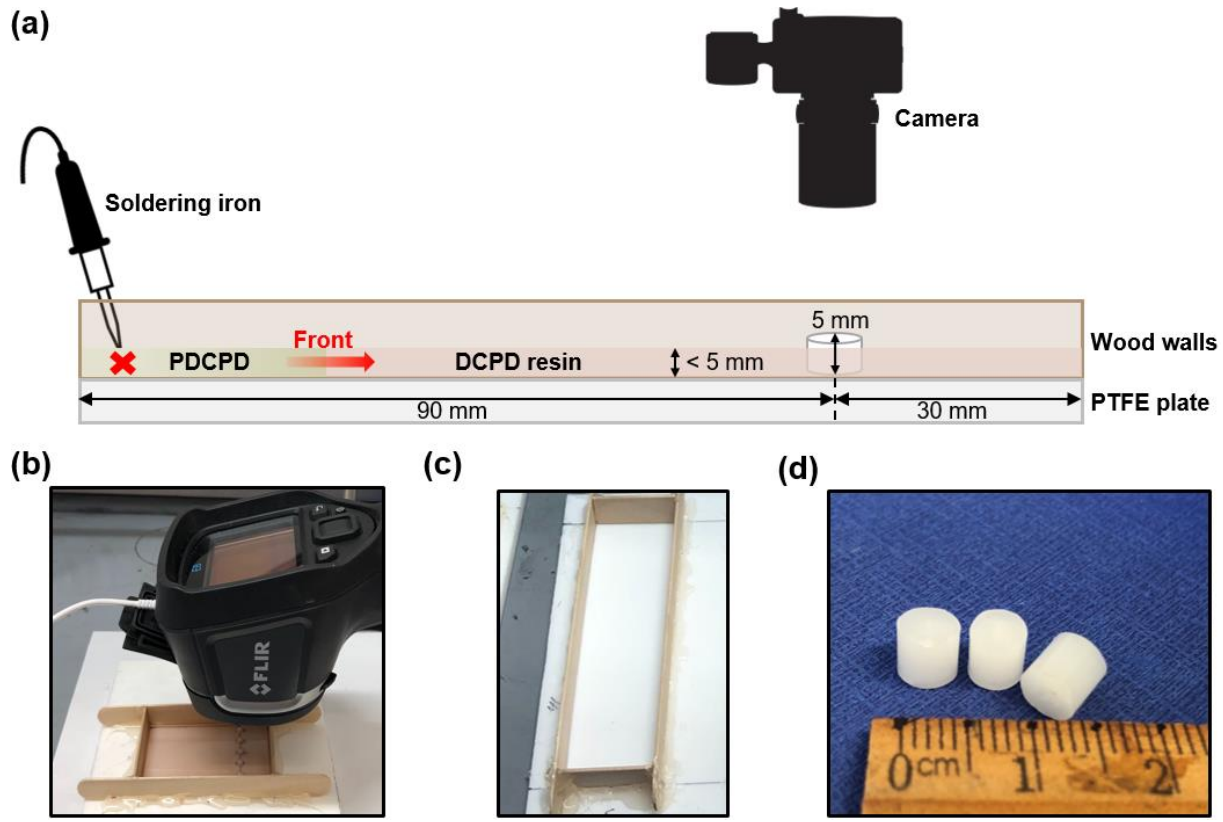

Figure A4. Experimental setup. a) Schematic and b) optic photo of the setup with the IR camera. c) Open mold used in the FP experiments. d) PCL cylindrical particles with r = 2.5 mm and height h = 5 mm.

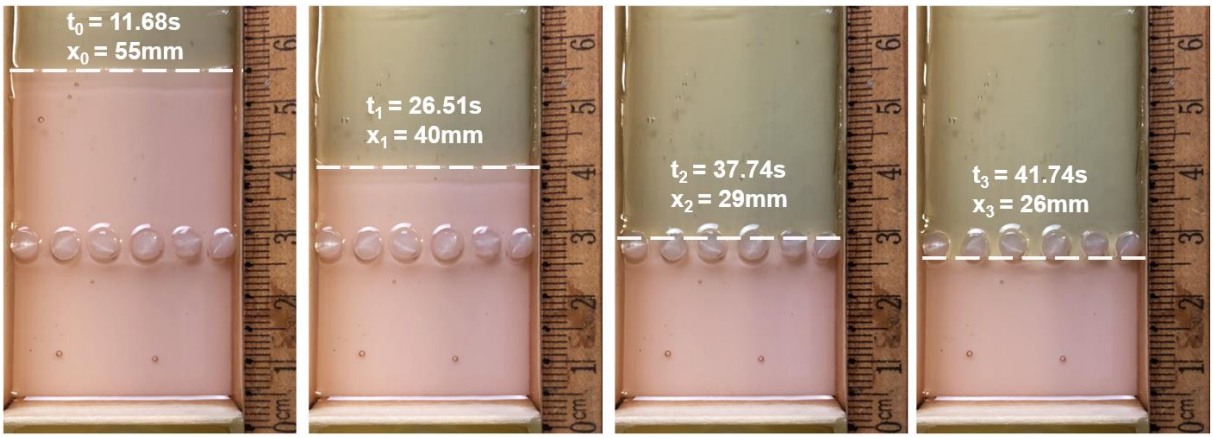

Figure A5. Extraction of the front velocity in experiments. Optical pictures of the propagation of the polymerization front (marked by white dashed lines) as it interacts with a row of six PCL particles. The front velocity is extracted from the time interval required for the front to propagate from one selected position to another. The steady-state velocity $v_\infty = (x_1 - x_0) / (t_1 - t_0)$. The interaction velocity $v_{int} = (x_3 - x_2) / (t_3 - t_2)$.

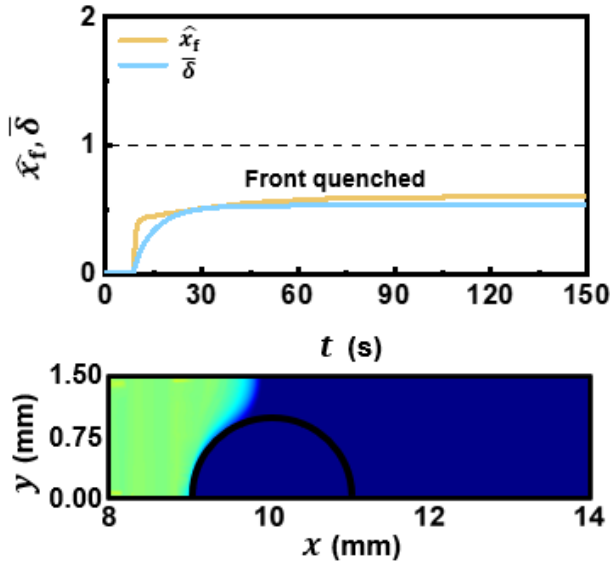

Figure A6. Quenched front due to convective heat loss. Relative position of the front $\widehat{x_f}$, average degree of melting $\bar{\delta}$ (top), and the front temperature T_f contours (bottom) confirm the quenching of the front due to convective heat loss, which gradually reduces the front temperature once the front is captured by the melting particles.

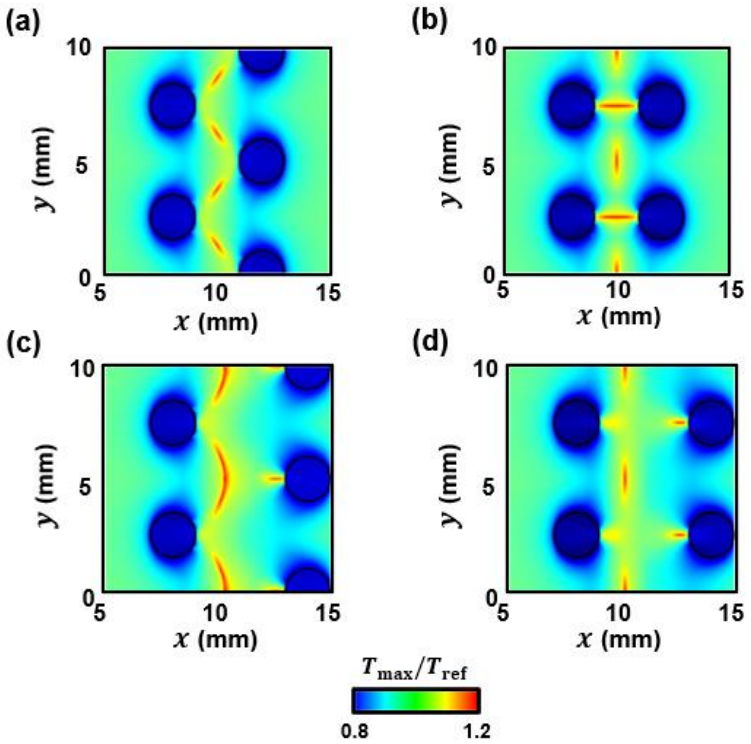

Figure A7. Symmetric a), b) and non-symmetric patterns c), d) achieved through the interaction of two polymerization fronts with two rows of particles.

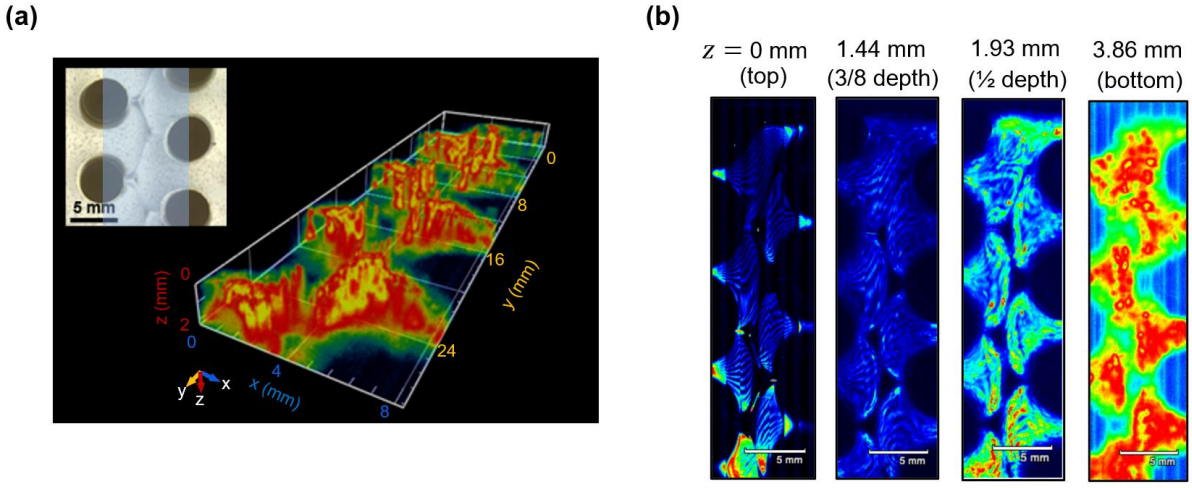

Figure A8. Confocal microscope scanning results. a) Maximum intensity view of patterns in the volume pictured in the inset. Half of the depth is shown. The signal intensity reflects the refractivity of the structure. b) Planar distribution of signal intensities at various depths (*z*-direction) from the top to the bottom of the sample. The zig-zag pattern visible at the surface persists through the thickness.

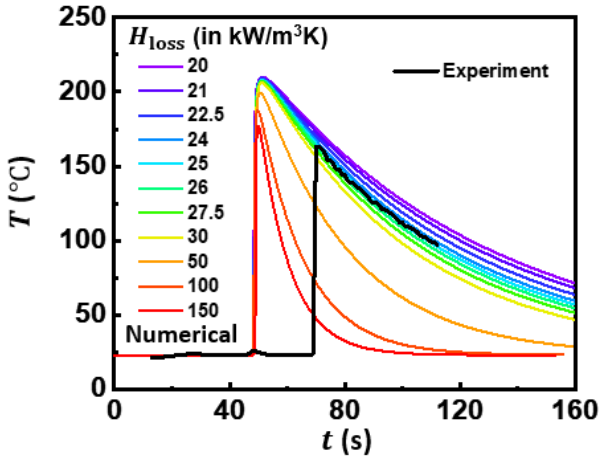

Figure A9. Temperature evolution in the path of a polymerization front. The rapid temperature rise associated with the front is followed by a slow decrease due to convective heat loss. The heat loss coefficient H_{loss} = 24.5 kW/m^3 is determined by matching experimental and simulated temperature decreases behind the front.

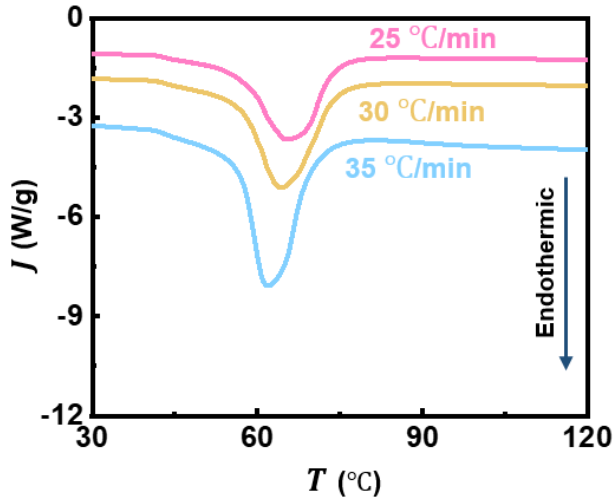

Figure A10. DSC measurements. Melting enthalpy of the PCL particles 82.3 ± 1.8 J/g measured by DSC tests.

Appendix B: Supporting Information for Chapter 3: Manipulating Frontal Polymerization and Instabilities with Phase-Changing Microparticles

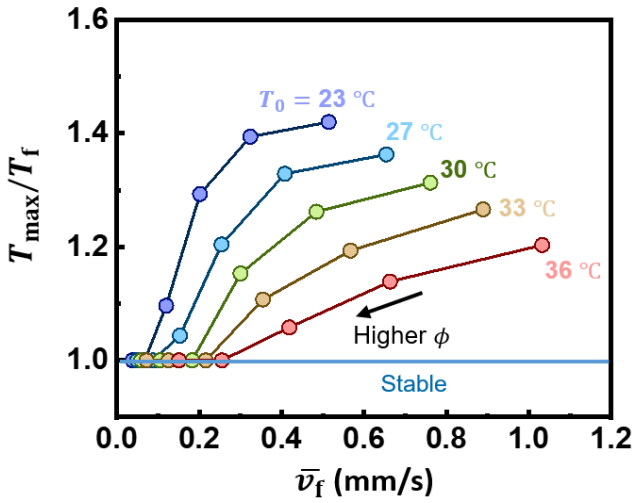

Figure B1. Temperature ratio T_{max}/T_f as functions of average front velocity $\overline{v_f}$ at various initial temperatures T_0. At a specific initial temperature T_0, a higher volume fraction of the PCL microparticles can reduces the instability (a temperature ratio close to 1) but compromises on $\overline{v_f}$. However, such compromise will be more acceptable at a higher T_0, where a higher $\overline{v_f}$ can be achieved at a given T_{max}/T_f (to the bottom-right of the graph).

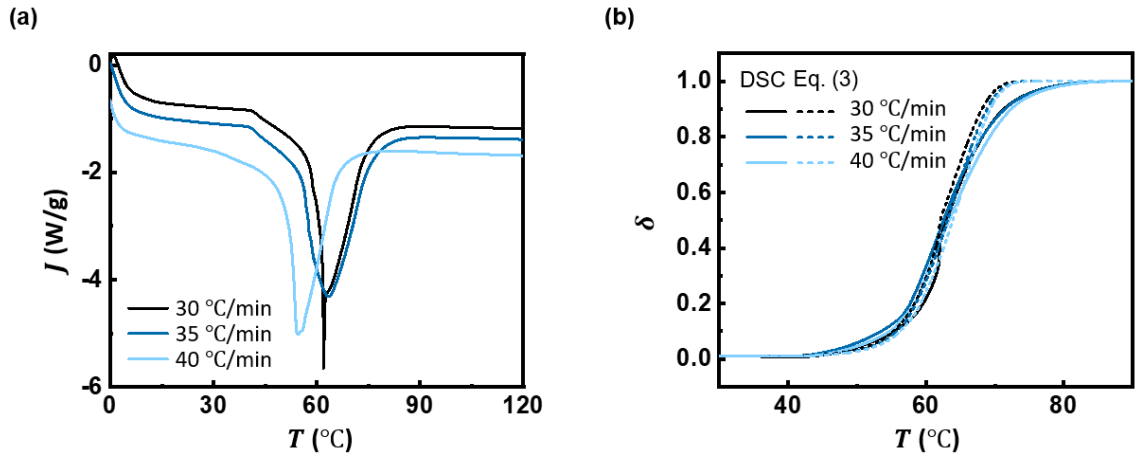

Figure B2. (a) DSC measurements of PCL microparticles at various ramping rates. The endothermic peaks indicate a melting enthalpy H_p of 89.0 ± 2.0 J/g. (b) Evolutions of the degree of melting in PCL microparticles measured in experiments and predicted by the melting kinetics model in (3) in the main text.